NUMERICAL ANALYSIS OF MAGNETOHYDRODYNAMIC PUMP

by

Wei Lin

Submitted in Partial Fulfillment of the Requirements

for the Degree of

Master of Science

in the

Mechanical Engineering

Program

YOUNGSTOWN STATE UNIVERSITY

August, 2011

NUMERICAL ANALYSIS OF MAGNETOHYDRODYNAMIC PUMP

Wei Lin

I hereby release this thesis to the public. I understand that this thesis will be made available from the OhioLINK ETD Center and the Maag Library Circulation Desk for public access. I also authorize the University or other individuals to make copies of this thesis as needed for scholarly research.

Signature:

_____
Wei lin , Student                                                                              Date

Approvals:

_____
Dr.Yogendra M. Panta, Thesis Advisor                                              Date

_____
Dr. Hyun W. Kim, Committee Member                                            Date

_____
Dr. Hazel Marie, Committee Member                                             Date

_____
Peter J. Kasvinsky, Dean of School of Graduate Studies and Research      Date

# ABSTRACT

Magneto-hydrodynamics(MHD) offers an elegant way to control fluid flow in micro devices without a need for any mechanical components. In the presence of an external magnetic field, the judicial interaction between the electric currents and magnetic fields results Lorentz forces in a microchannel filled with ionic sample solutions and patterned with electrodes on the opposing walls. The resulted Lorentz forces can be used to propel, stir, mix and/or manipulate fluid in the channel. So far, many works are reported about the MHD micro channels for various applications. There is still a need for better understanding of flow behavior in these microdevices. Also, there are insufficient studies of flow phenomenon under MHD in microtubules.

In this thesis, microchannels are designed and modeled to run 3D fluid flow simulation for MHD investigation. Rectangular microchannels' geometries in the order of micrometers were created, preprocessed, simulated and postprocessed in COMSOL, a commercially available finite element software. COMSOL is used here to model the fluid flow through Navier-Stokes and chemical ion transport through Nernst-Planck principles. With and without the application of external magnetic field, the fluid flow rate through the exit port was observed higher for B=0.44T than without any magnetic field for B=0. In the presence and absence of external magnetic fields, an extensive parametric study was performed in order to find out the cross

dependencies within the various experimental parameters. Logical and numerical conclusions were drawn from this study to prove the concept of MHD for manipulating fluid flow parameters in tubular microchannels. Simulation results were compared and found in a good agreement with published experimental data in order to validate the computational study aforementioned.

# ACKNOWLEDGMENTS

I would like to express my deepest gratitude to my advisor Dr. Yogendra M. Panta for the continuous support of my study and research as a graduate student. His guidance, extreme patience and long suffering, ideas, and opinions helped me immensely throughout this thesis. My special thanks to Dr. Hyun W. Kim and Dr. Hazel Marie for having accepted the task of serving on my thesis committee, helping me in proofreading, and providing important suggestions. I would like to thank my classmate and dear friends Anthony Solic , Rani Kummari, Looja Tuladhar, Fei Wu, Zhaoxin Wang, Sai Atmuri, Sunket Aryal and  Param Adhikari for their unforgettable friendly support and help.

Also I would like to give my endless thank my family , my father Dichun Lin, my sister Zi Lin and Nana Lin for their encouraging suggestions and help. Without your love and support none of this would have ever been possible.

Finally I would be amiss for not being grateful to the supreme being, my heavenly mother Meirong Wang for the opportunity and mercy I know in my heart I have been given to remain on this earth to learn, discover and progress. Although I am often burdened with my inadequacies, medical conditions and character flaws, I know who to turn to for help in these matters and I hope to do and become as she want me to be.

**TABLE OF CONTENTS**

# LIST OF FIGURES

# LIST OF TABLES

# CHAPTER 1

# INTRODUCTION

## 1.1 Lab-on-a-chip Technology

In recent years, there has been a growing interest of research in studying and developing Lab-on-a-chip (LOC) technology for varieties of applications. Lab-on-a-chip is a minute chemical processing plant which integrates most common laboratory procedures like filtration, mixing, separation and detection in a single chip. All these laboratory operations can be programmed within a single chip of only a credit card size or even smaller. The interconnected networks of micro-nano channels and reservoirs with tiny volumes of samples are well matched with the demands for small sample volume, low cost, rapid response, and massive parallel analyses, Figure 1.1.
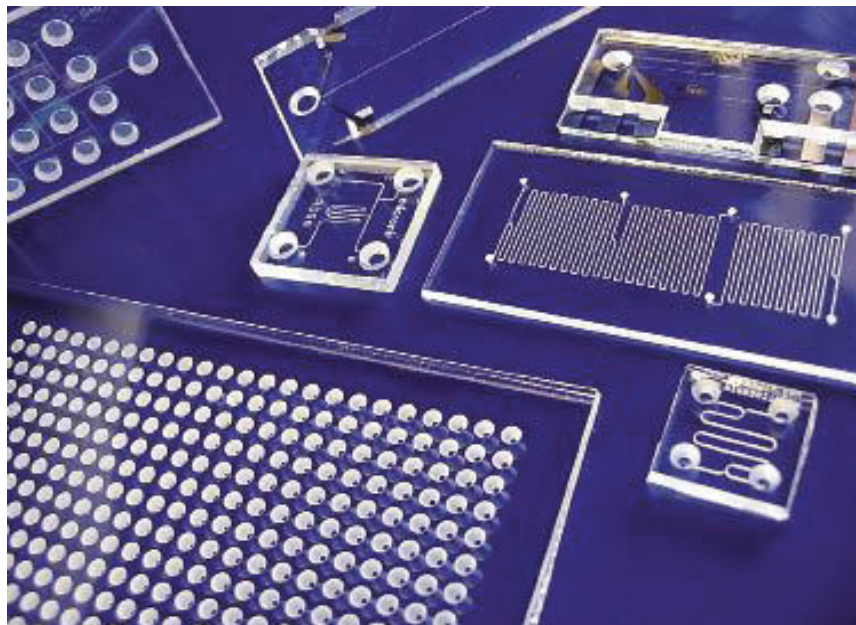


**Figure 1.1.** Lab-on-a-chip Models

## 1.2 Fluid Propulsion in LOC

Many LOC devices require to propel fluids transporting samples between various ports, stir to enhance mixing, control and manipulate fluid motion and separate fluids (Terray et al., 2002). For all these operations, fluid propulsion is one of the main problems associated with these devices. Over the past several years, many techniques for manipulating the fluid propulsion in microchannels have been proposed. This thesis focuses on properly oriented use of magnetic and electrostatic forces to generate magneto hydrodynamic effect of fluid flow for pumping fluids in micro-conduits. Below is a brief summary of various means of propelling fluids in lab-on-a-chip devices.

### a) Pressure-driven flow

Pressure-driven flow in LOC devices is a fluid propulsion method by using external pumps, on chip integrated pumps, or compressed gas (*Kopp et al., 1998; Fu et al., 2002; Park et al., 2003*). Pressure-driven flow has the ability to produce high flow rates in micro-channels. This method is used in many microfluidic systems like flow cytometry, to achieve higher flow rates in the channels even with only a few hundred micrometers length (*Fu et al., 2002*). The pressure driven flow is a Poiseuille flow characterized by a parabolic velocity profile. The main disadvantage of this type of flow is dispersion. Interaction between convection and diffusion is found important in many applications, especially those with chemical and biological reactors.

**b)      Electrokinetically Driven Flow**

There are three kinds of electrokinetically driven flow phenomena associated with the propulsion of fluids: electro-osmosis, electrophoresis and di-electrophoresis (*Probstein, 1*994). First, the electro-osmotic phenomenon is caused by the formation of a net electric charge on the solid's surface that is in contact with the electrolyte solution and the accumulation of mobile counter ions in a thin liquid(double electric or Debye) layer next to the solid's surface. The electrolyte behaves neutral when it is away from the solid's surface. With an external electric field, the counter ions in Debye layer are attracted to the oppositely charged electrode and drag the liquid along. In other words, the electric field creates a body force through its effect on the counter ions, which, in turn, induces fluid motion. As the body force is concentrated in a very small area next to the solid boundaries, so the velocity profile due to the electroosmotic flow is almost uniform and flat.

Second, electrophoresis refers to the movement of charged particles under external applied electric field, and it has been widely used to separate large molecules (such as DNA fragments or proteins) from a mixture of similar molecules. In the presence of electric field, various molecules travel through the medium at different rates, depending on their electrical charge and size. The separation is based on these differences. Agarose and acrylamide gels are commonly used for electrophoresis of proteins and nucleic acids. An uncharged conducting object suspended in a solution subject to electric field is polarized. When the electric field is non-uniform, this results in a dipole moment. Due to the interactions between the electric dipole and the

gradient of the electric field, the object migrates in the solution. This phenomenon is called dielectrophoresis (DEP). DEP has been used to trap cells, beads, nano-tubes or other targets to be selectively manipulated or held in a place when washed(*Arai et al., 2001; Wheeler et al., 2003*). However, the successful application of DEP to separation problems demands awareness of a number of confounding factors such as the polarization of the double layer, electrode polarization, thermal convection, and wide range of particle characteristics under different AC electric field frequency(*Gascoyne and Vykoukal,2002*).

One of the main advantages of using electric field induced flows is to avoid the moving parts for transporting fluid in the system. But the flow rates induced from electrostatic forces is very low and consequently a very low Reynolds's number application and the usage of high electric fields is required. Besides these, internal heat generation (commonly referred to as Joule heating) which is created by the current flows through the buffer solution with high electric fields ( *Erickson et al., 2003*) is another drawback.

**c)    Surface tension-driven Flow**

Because the characteristic length scale of microfluidic systems is very small, surface forces are accounted for the main role to manipulate the flow. The surface forces are used to drive a liquid droplet by modifying the contact angle of the drop with the solid surface where it lands (*Vladimirova et al., 1999; Zhao et al., 2001; Erickson et al., 2002; Mauri et al., 2003; Stange et al., 2003*). Contact angle can be modified by electro-wetting. In addition, capillary forces can also be used to fill dry

conduits. For instance, lateral flow reactors use this mechanism to move the reagents to detection site. For this propulsion method, no external driving force is required. However, this phenomenon makes the flow direction and flow rate are very difficult to control and the process terminates once the dry conduits are fully saturated.

**d)** **Centrifugally Driven Flow**

When the device is rotated such as in the case of a lab-on-a-CD, one can obtain very high accelerations, and fluid motion results. One can control the flow by adjusting the angular rotation speed and the position of the component within the device. However, fluids can only move in the direction of the centrifugal force (*Johnson et al., 2001; Chen et al., 2004*).

**e)** **Buoyancy-driven Flow**

Since the length scales and the temperature variations in microfluidic devices are very small, buoyancy effects are generally negligible. However, certain processes such as thermal Polymerase Chain Reaction (PCR) for DNA amplification need large temperature variations to achieve significant flow velocities even in micro conduits. Recently, Krishnan et al.,(2002) used this effect to create naturally occurring circulation in a cavity heated from below and cooled from above (the Rayleigh-Benard cell) to circulate reagents between two different temperature regimes. Chen et al.,(2004) significantly improved this concept by closed loop thermosyphon (*Krishnan et al., 2002; Chen et al., 2004*).

**f)      Magneto-hydrodynamics(MHD) Flow**

Magnetohydrodynamics (MHD) (magneto fluid dynamics or hydromagnetics) includes the study of the dynamics of electrically conducting fluids under the effect of magnetic field (*Woodson and Melcher et al.,1969; Bau et al., 2003; Qian et al., 2005;Homsy et al., 2007; Fatemeh et al., 2011)*. Examples of such fluids include plasmas, liquid metals, and salt water or electrolytes. The field of MHD was initiated by Hannes Alfvén in 1970. The set of equations which describe MHD are a combination of the Navier-Stokes equations of fluid dynamics and Maxwell's equations of electromagnetism. Besides these, the presence of electrically conducting ions in the fluid domain requires to couple the physics of fluid with the physics of ion transport in the fluid flow. These differential equations have to be solved simultaneously, either analytically or numerically.

In microfluidic devices, it is necessary to propel samples and reagents from one part of the device to another, stir fluids, and detect the presence of chemical and biological targets.  Given the small size of these devices, the above tasks are far from trivial.

In a recent review article, it has been reported that magnetohydrodynamics (MHD) offers an elegant means to control fluid flow in microdevices without a need for mechanical components such as fluid pumping, flow control in fluidic networks, fluid stirring and mixing, circular liquid chromatography, thermal reactors, and microcoolers (Qian etal, 2009). Some of the advantages of MHD technique include no-moving parts, portable, economic, and versatile. This thesis work presented here

mainly focuses on the development of micro pumps utilizing magnetohydrodynamic action. Below is a summary of various means of fluid propulsion along with their brief description, advantages and disadvantages as shown in Table 1.1.

**Table 1.1.** Various means of fluid propulsion (Juan Katoff,2007)

| Means | Description | Advantages | Disadvantages |
|---|---|---|---|
| **Pressure** | Fluid motion is induced by pressure difference. | High flow rate; No moving part | Need a mechanical pump; High pressure |
| **Electroosmosis** | Fluid motion is induced by electrostatic force. | Uniform velocity No moving part | Low flow rate; High electric field; Depends on the characteristics of the liquid-solid interface |
| **Surface tension** | Fluid motion is induced by surface tension. | No external driving force; No moving part | Difficult to control the flow rate and direction |
| **Centrifugal force** | The device is placed on a rotating platform. | High flow rate | Fluids move only in one direction |
| **Buoyancy** | Fluid motion is induced by the dependence of fluid density on the temperature variations. | Self-accurate; No moving part; Simple | Large temperature variations are required. |
| **MHD** | The motion is induced by the interactions between electric and magnetic fields. | Low cost; Low electric field; Reasonable flow rates; No moving part. | Electrode erosion; Bubble formation; |

## 1.3 Magnetohydrodynamics (MHD) Flow

LOC is a minute chemical processing plant that integrates common laboratory procedures ranging from filtration and mixing to separation and detection. The various operations can be programmed and performed automatically within a single chip platform. To achieve these various laboratory tasks, it is necessary to propel, stir, mix, manipulate and control the fluid motion within the micro-conduit. Since in many applications, one uses buffers and analyte solutions that are electrically conductive, then one can transmit electric currents through the bulk solutions with the sidewalls that can be patterned across the channel walls. In the presence of an external magnetic field, the interaction between the electric currents and magnetic fields results Lorentz forces, which, in turn, can be used to propel and manipulate fluids, Figure 1.2.
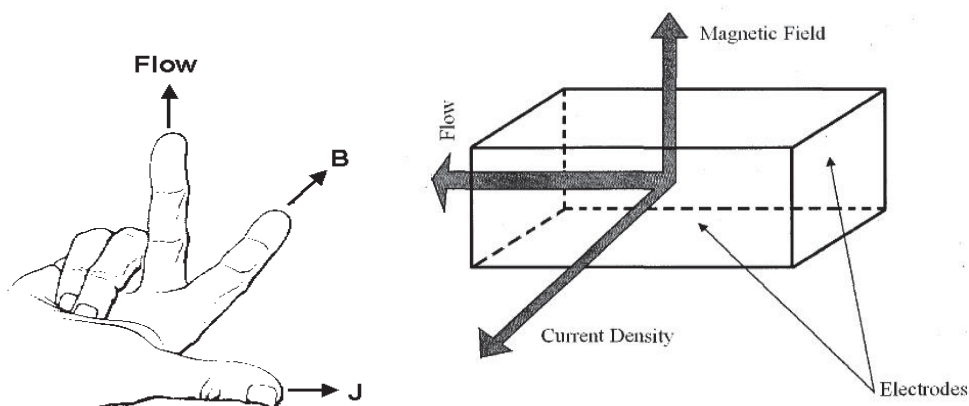


**Figure 1.2.** Interactions between the Magnetic Field and the Induced Current

Applications of MHD effect in microfluidics to pump, propel and control fluids or ionized gases are well-known *(Woodson and Melcher, 1969; Davidson, 2001)*. Recently, various MHD based microfluidic devices including micro pumps *(Jang and Lee, 2000; Lemoff and Lee, 2000; Huang et al., 2000; Bau, 2001; Zhong et al., 2002;*

*Bau et al., 2002, 2003; Sawaya et al., 2002; West et al., 2002, 2003; Ghaddar and Sawaya, 2003; Bao and Harrison, 2003a, 2003b; Eijkel et al., 2004; Wang et al, 2004; Arumugam et al., 2004, 2006; Qian and Bau, 2005b; Homsy et al., 2005, 2007; Affanni and Chiorboli, 2006; Aguilar et al., 2006; Kabbani et al., 2007; Patel and Kassegne, 2007; Duwairi and Abdullah, 2007; Ho, 2007)*, stirrers *(Bau et al., 2001; Yi et al., 2002; Qian et al., 2002; Gleeson and West, 2002; Xiang and Bau, 2003; Gleeson et al., 2004; Qian and Bau, 2005a)*, networks *(Bau et al., 2002, 2003)*, heat exchangers *(Sviridov et al., 2003; Singhal et al., 2004; Duwairi and Abdullah, 2007)*, chemical analytical devices and biomedical devices *(Leventis and Gao, 2001; West et al., 2002, 2003; Bao and Harrison, 2003a; Lemoff and Lee, 2003; Eijkel et al., 2004; Clark and Fritsch, 2004; Homsy et al., 2007; Gao et al., 2007; Panta et al., 2008)*, heavy metal iron($Hg^+$) detection *(Panta and Qian et al., 2009)* and radionuclides detection *(Panta and Farmer et al., 2010)* operated either by DC or by AC electric fields were reported. When we operate the device with DC source, bubble formation and electrode corrosion are two main problems due to the chemical reaction between the electrode material's and the analyte samples leading to the production of foreign chemical compounds in the bulk solution. These problems can be solved by using AC fields instead of DC fields, however, AC operation requires electromagnets instead of the permanent magnets which are used in DC operation, the change may result increasing power consumption.

MHD driven flow is the most efficient way of manipulating and controlling fluids inexpensive, versatile, without any moving parts, and portable compared to

other means of fluid flow. Specifically, MHD based LOC devices can be operated at very low voltages (<1V usually in millivolts) with no moving. MHD based fluid flow was successfully applied in order to ultra-detect mercury and radionuclides as shown in the figures below and referred earlier, Figure 1.3.
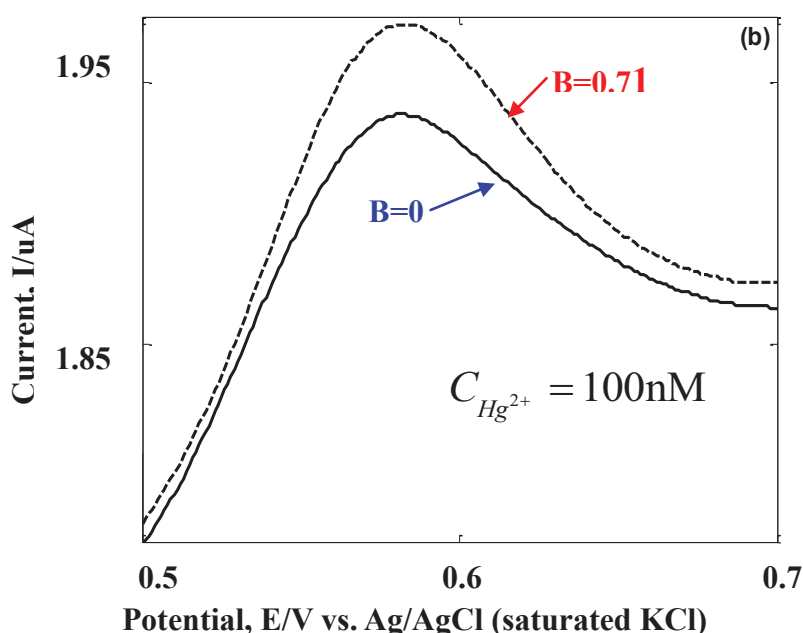
**Figure 1.3.** MHD convection used for ultra-detection of $Hg^{2+}$ by using electrochemical method. (Yogendra M. Panta, 2008)

However, as previously mentioned, there are also some disadvantages of MHD driven flow, such as bubble formation, electrode corrosion, and migration of analyses in the electric field. The introduction of RedOx species into the liquid is a potential solution to the problems associated with the DC MHD micro fluids.

**1.4 Reduction-Oxidization based Magnetohydrodynamics (RedOx-MHD) Flow**

RedOx MHD is a recently developed technique that is becoming a novel means to pump or manipulate fluid motion in microchannels for several reasons: high reliability, no external moving parts, and operable under low voltages compared to MHD without

RedOx electrolytes. RedOx MHD couples the MHD flow in presence of RedOx chemicals confined in the solution. In addition, Redox MHD is a novel method suitable for micro volume pumping or mixing in portable devices or in high-throughput analyses because of its versality with no moving parts, reversible flow direction, and low voltages applications. An external magnetic field (from an electromagnet or compact, permanent magnets), coupled with the electrochemical oxidation or reduction of a RedOx species in solution, results in a Lorentz force which acts on current-carrying species in solution and leads to bulk convection. Therefore, enhancements in electrochemical currents are observed in the presence of a magnetic field due to increased mass transport to the electrode (*Anderson*, 2006).

Assuming the fluid flow is steady state and the ionic fluid is incompressible, the velocity profile in RedOx MHD flow can be seen as follows, Figure 1.4.
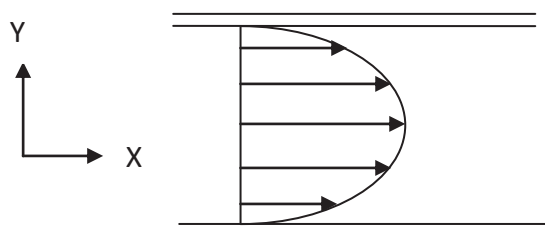


**Figure 1.4.** Velocity Profile as is observed in MHD Flows within Microchannels

Some of advantages of RedOx MHD pumping are follows:

1.      Economic

2.      Needs low potential field

3.      No moving parts

4.      Pumps high mass flow rates

5.      Repeatable results,

6.      Consumes less power

There are still two main draw backs in RedOx MHD flow. One, when high voltages are applied, the current will increase. The increase in current may lead to faster ionic reaction and consequently speeding up the electrolysis process. That means bubbles may be created and can eventually block the fluid flow. Two, the electrodes' life span can be relatively shorter, needing to replace electrodes frequently.

In this thesis, three dimensional simulation of RedOx MHD flow in a microchannel is performed with different chemical transport phenomena; fluid and ionic domain parameters and boundary conditions are presented and analyzed. The inter relationship among those variables are discussed and explained.

## 1.5 Thesis Structure

Thesis contents are structured with chapter one that includes an introduction to MHD and Lab-on-Chip technology. Following chapter one, study of physical and mathematical modeling of microchannels is presented in chapter two. Chapter three covers the numerical modeling of various microchannels. Results and discussion are presented in chapter four. Chapter five concludes with possible future works.

# CHAPTER 2

# MODELING OF MICROCHANNELS

To understand the MHD driven fluid flow in microchannels, rectangular cross sectioned microchannels with various shapes were studied. Following the introduction and the overview of MHD driven fluid flow, modeling of various microchannels are presented in this chapter. Modeling includes the geometrical modeling of various shapes of microchannels including a straight rectangular microchannel, converging microchannel, and diverging microchannels.

## 2.1    Geometrical Modeling

A micro-conduit having micro scale dimensions for its height and width with a mille scale dimension for length was selected to study MHD fluid flow by both three dimensional and two dimensional(Qian et al, 2002) analysis. As shown below in Figure 2.1(a), a rectangular cross sectioned microchannel with length L=18mm, width W=330μm, and height H=670μm were used to create the geometrical modeling in Solid Works. In order to compare the pumping efficiency of straight microchannel, two other microconduits with converging and diverging shapes were created as shown in Figure 2.1(b) and Figure 2.1(c) respectively.
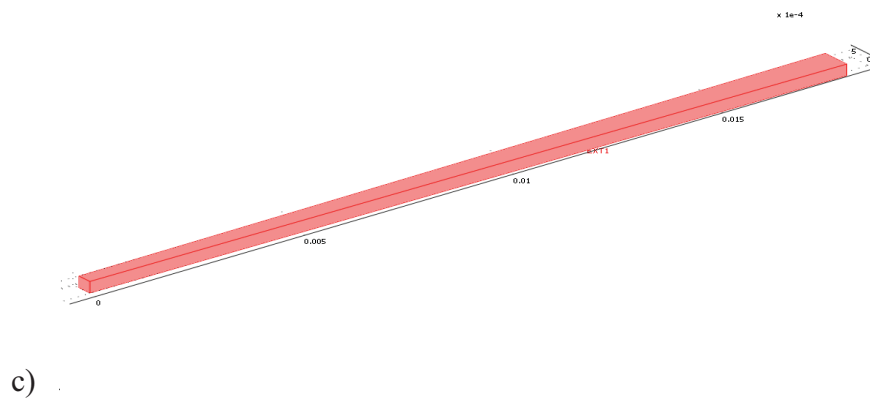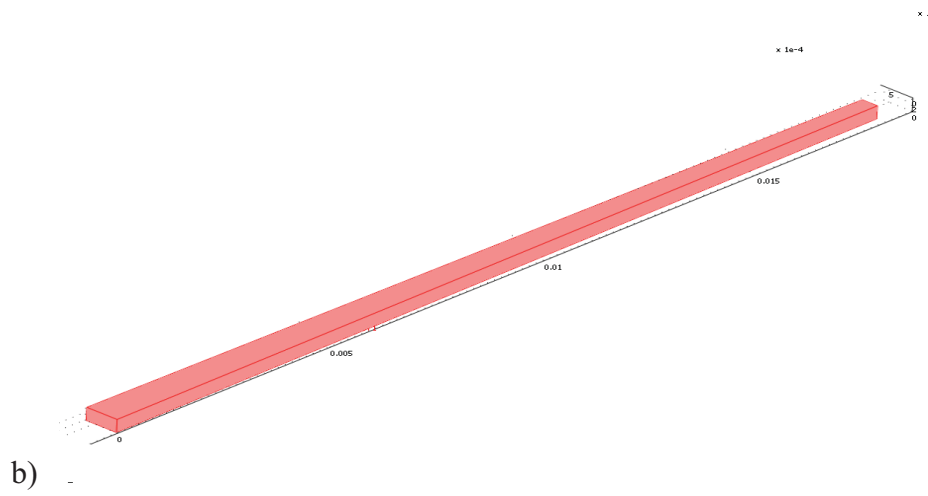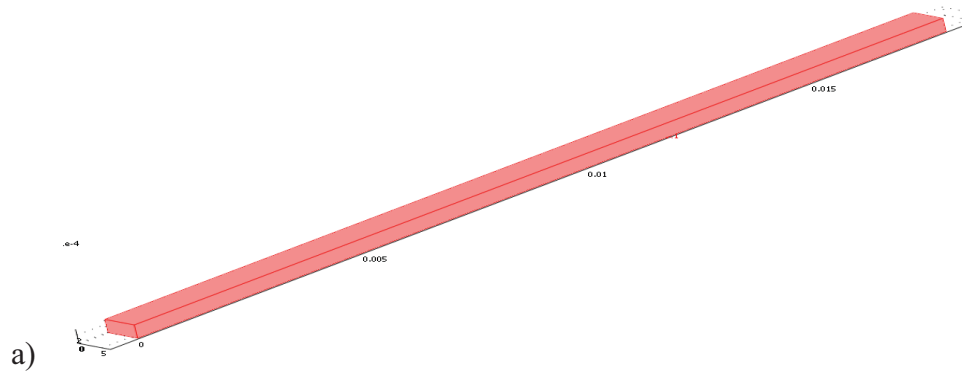
**Figure 2.1**. Geometrical Modeling of (a) Straight (b) Converging, and (c) Diverging Microchannels

As shown above in **Figure 2.1(b)**, a rectangular cross sectioned microchannel with inlet cross sectional area; width W=330μm × height H=670μm and outlet cross sectional area; width W=330μm × height H=335μm were created in Solid Works, a geometrical modeling software.

Similarly, as shown in **Figure 2.1 (c)**, a rectangular cross sectioned microchannel with inlet cross sectional area; width W=330μm × height H=670μm and outlet cross sectional area; width W=330μm × height H=1340μm were created in Solid Works, a geometrical modeling software.

Due to the MHD effects, ionic fluid is pushed forward from the inlet to the outlet developing the velocity profiles over the length of the channel. There were two schemes of modeling various other microchannels with respect to a straight rectangular microchannel which was assumed as a control model. One, inlet cross sectional areas are maintained the same in all the microchannel models to do a comparative study of their outlet velocities. Two, outlet cross sectional areas are maintained the same in all the microchannel models to do a comparative study of their inlet velocities. This would deliver a clear understanding of how the velocity profiles, average velocity and the maximum axial velocity change with respect to the channel height for each of the three microchannels from their inlet to mid- and to the outlet. It should be noted that the height to the width (H/W) ratio of the straight, diverging and converging channels from the inlet reservoir to the outlet reservoir are, respectively, 1 to 1, 1 to 2, and 1 to 1/2 . Two different approaches are considered to determine the effectiveness of the MHD effects in straight, diverging and converging microchannels

and the models are shown in Figure 2.2.
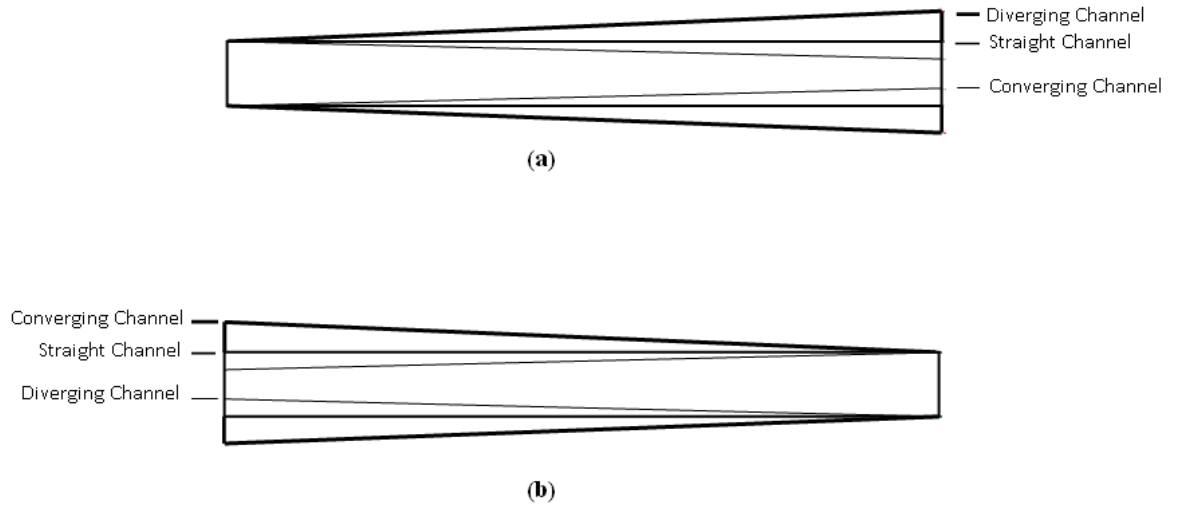


**Figure 2.2.** Three microchannel models keeping the (a) inlet cross sectional area same in all models (b) outlet cross sectional area same in all models.

## 2.2    Mathematical Model

While mathematically modeling the electrically conducting fluid flow in the micro-conduits, two main multiphysics, physics of fluid flow and physics of ionic mass transport, are coupled together resulting the higher fluid pumping.   The orthogonal interaction of magnetic field with the electric field generated across the electrode walls in the microchannel induces the Lorentz force. Lorentz force is included as a body force in the momentum equation while modeling the physics of fluid flow. In other words, physics of fluid flow in the confined micro-conduit's domain are governed by continuity and momentum (Navier-Stoke) equations including the induced Lorentz force as a body force. Similarly, physics of ionic mass transport are governed by a series of equations, namely Nernst-Planck equation for

16

the conservation of mass transport of chemical species and Butler-Volmer equation for electrical current vs. electric potential for each current carrying species. Butler-Volmer equation shows the dependency of electrical current on an electrode potential for each current carrying species in the bulk solution. The coupling of these two physics completes the mathematical modeling of the MHD flow in microchannel. Mathematical expressions for a three-dimensional microchannel as shown in Figure 2.3 (revisited in chapter 4) are explained later.

Following the physical model as explained before, both MHD and Redox MHD flow were mathematically analyzed and compared in the given micro-conduits. As explained earlier, the fluid domain can be expressed further by a combinational approach of physics of ionic mass transport coupled with physics of fluid flow.

A Cartesian coordinate system is used with its origin located at left front corners of the 3D channel as shown in Figure 2.3. X, Y, and Z are along the channel's length, width, and height ($0 \leq x \leq L$, $0 \leq y \leq W$, and $0 \leq z \leq H$) respectively. Two planar electrodes are patterned on two opposing walls with length of $L_s$ and height of H, here we make $L_1 = 0$ and $L_s = L$ so the electrodes are applied along the entire wall length. This conduit is filled with RedOx electrolyte solution under magnetic field. When a potential difference V across the electrodes is applied, the electrodes from both walls induce a current density **J** due to electron transfer, and we assume the device is placed under a permanent magnet with a magnetic flux density **B**.
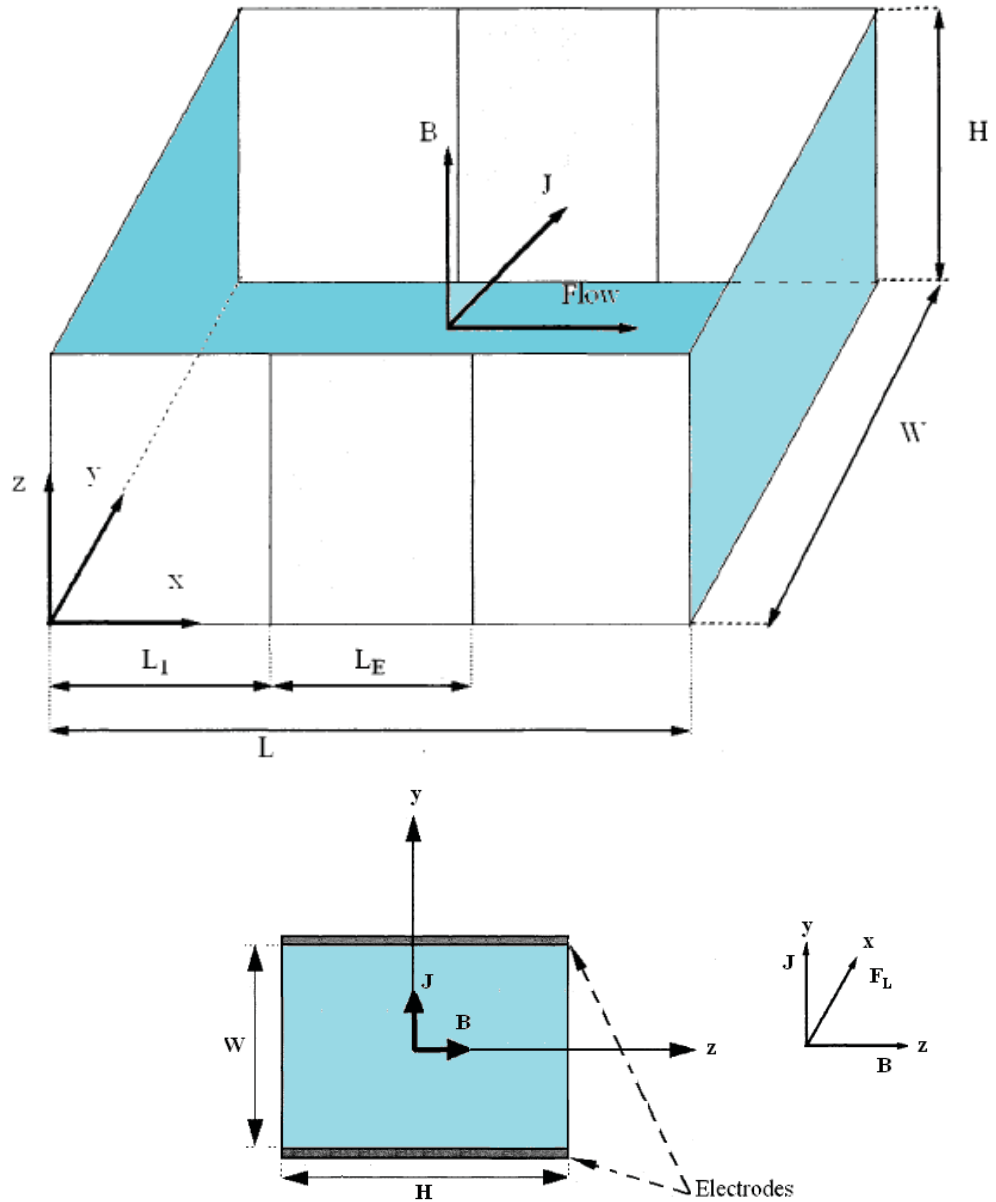
**Figure 2.3.** Schematics of a three-dimensional, planar microchannel patterned with two electrodes along the opposite walls of the micro-conduit which is filled with a dilute RedOx chemical species $K_4[Fe(CN)_6])$ and $K_3[Fe(CN)_6]$ that is subjected to a uniform magnetic field of flux density B. A potential difference $\Delta V$ is imposed across the electrodes resulting in a current density J which then oriented orthogonally with the magnetic field to induce the Lorentz forces. The Lorentz forces pump the ionic fluid from the inlet reservoir to the outlet reservoir through the conduit.

An orthogonal interaction between the current density and externally applied magnet flux density induces Lorentz force which eventually creates the fluid flow, Lorentz force is represented as $F_L$ and expressed as follows:

$$F_L = J \times B \tag{2.1}$$

$$F_L = (J_x\,\mathbf{e}_x + J_y\,\mathbf{e}_y + J_z\,\mathbf{e}_z) \times (B_x\,\mathbf{e}_x + B_y\,\mathbf{e}_y + B_z\mathbf{e}_z) \tag{2.2}$$

$$F_L = (J_x\,\mathbf{e}_x + J_y\,\mathbf{e}_y + 0\,\mathbf{e}_z) \times (0\,\mathbf{e}_x + 0\,\mathbf{e}_y + B\mathbf{e}_z) \tag{2.3}$$

$$F_L = -\,J_xBe_y + J_yBe_x + 0e_z. \tag{2.4}$$

In the above expression, $J_x$ and $J_y$ are, respectively, the x and y component current densities, $e_x$ and $e_y$ are, respectively, the unite vectors in the x and y directions. $B_x=0$, $B_y=0$ and $B_z=B$, respectively, the x and y component magnetic flux densities.

### 2.2.1      Mathematical Model of Fluid Flow

The mathematical models consist of a set of governing equations that are used for a closed-form solution and are also embedded within COMSOL 3.5a to analyze and describe the physical phenomena in a given fluid domain.  There exist multiple governing equations that each has their own given characteristics to solve for certain values that are based upon the user's interest.  The purpose of this chapter is to introduce and describe the governing equations of the fluid domain.

The three equations used are the continuity, momentum, and later developed as the generalized Navier-Stokes equations.

- Incompressible flow – for negligible change in density of air flow

- Steady flow – as time dependent analysis is not considered.

- Newtonian fluid -  wind having Newtonian fluid behavior for shear stress

### a)  Continuity Equations

The law of conservation of mass for fluid flow states that the rate of mass

leaving a control volume is equal to the rate of mass entering the control volume. In other words, mass is always conserved in a control volume. The statement, expressed mathematically is shown in Equation 2.5 which is further reduced into Equation 2.6.

$$\frac{\partial \rho}{\partial t} + \nabla \cdot \left( \rho \vec{V} \right) = 0$$

(2.5)

Where,

$\dfrac{\partial \rho}{\partial t} \equiv$ rate of change of density within the control volume

$\nabla \equiv$ vector operator in Cartesian coordinates $= \dfrac{\partial}{\partial x} \hat{i} + \dfrac{\partial}{\partial y} \hat{j} + \dfrac{\partial}{\partial z} \hat{k}$

$\nabla \cdot \left( \rho \vec{V} \right)$ flow across boundaries of the control volume

For incompressible flow, the continuity equation reduces to:

$$\nabla \cdot \left( \rho \vec{V} \right) = 0$$

(2.6)

**b) Momentum Equations**

The conservation of momentum equation is obtained by applying principles of Newton's second law of motion to the fluid domain. Newton's second law states that the net force on a particle, or an object, is equal to the time rate of change of its linear momentum. This law can be applied to a fluid particle moving through 3-dimensional space. The result is three equations, each with respect to the x-,y-, and z- directions as shown in Equations 2.7-2.9. Basically, the net force on the particle, or object, in the x- direction is equal to the time rate of change of its linear momentum in the x- direction. The same holds true for the y- and z- directions. The law, in mathematical terms, with

respect to the three coordinate axes (x, y, z) is as follows:

$$\frac{\partial(\rho u)}{\partial t} + \nabla \cdot \rho \vec{V} u = dF_{Bx} + \frac{\partial \sigma_{xx}}{\partial x} + \frac{\partial \tau_{yx}}{\partial y} + \frac{\partial \tau_{zx}}{\partial z} + S_{Mx} \qquad (2.7)$$

$$\frac{\partial(\rho v)}{\partial t} + \nabla \cdot \rho \vec{V} v = dF_{By} + \frac{\partial \tau_{xy}}{\partial x} + \frac{\partial \sigma_{yy}}{\partial y} + \frac{\partial \tau_{zy}}{\partial z} + S_{My} \qquad (2.8)$$

$$\frac{\partial(\rho w)}{\partial t} + \nabla \cdot \rho \vec{V} w = dF_{Bz} + \frac{\partial \tau_{xz}}{\partial x} + \frac{\partial \tau_{yz}}{\partial y} + \frac{\partial \sigma_{zz}}{\partial z} + S_{Mz} \qquad (2.9)$$

Where,

$\vec{V} \equiv$ total velocity vector of the fluid

$u, v, w \equiv$ x-, y-, and z-components of the velocity, respectively

$\sigma_{ii} \equiv$ normal viscous stress terms

$\tau_{ij} \equiv$ shear viscous stress terms

$dF_{Bi} \equiv$ differential body force component

$S_{Mi} \equiv$ momentum source term component

## c) Navier-Stokes Equations

The viscous stresses and the rate of angular deformation, or in other words the rate of shearing strain, are directly proportional to one another for a Newtonian fluid. Since air is considered to be a Newtonian fluid, it is possible to express the viscous stresses in terms of velocity gradients. These expressions are below:

$$\tau_{xy} = \tau_{yx} = \mu\left(\frac{\partial v}{\partial x} + \frac{\partial u}{\partial y}\right) \qquad (2.10)$$

$$\tau_{yz} = \tau_{zy} = \mu\left(\frac{\partial w}{\partial y} + \frac{\partial v}{\partial z}\right) \qquad (2.12)$$

$$\sigma_{xx} = -p - \frac{2}{3}\mu \nabla \cdot \vec{V} + 2\mu\frac{\partial u}{\partial x} \qquad (2.13)$$

$$\sigma_{yy} = -p - \frac{2}{3}\mu\nabla\cdot\vec{V} + 2\mu\frac{\partial v}{\partial y} \qquad (2.14)$$

$$\sigma_{zz} = -p - \frac{2}{3}\mu\nabla\cdot\vec{V} + 2\mu\frac{\partial w}{\partial z} \qquad (2.15)$$

Where, $p \equiv$ local thermodynamic pressure

$\mu \equiv$ dynamic or absolute viscosity of the fluid

It should also be noted that the kinematic viscosity, $\upsilon$, can be substituted for $\mu$, the ratio of the dynamic viscosity of the fluid by its density, $\rho$.

The kinematic viscosity equation is shown in Equation 2.16.

$$\upsilon = \frac{\mu}{\rho} \qquad (2.16)$$

Equations of viscous stress, Equations 2.10–2.15, are then combined with the differential equations of motion, Equations 2.7–2.9, resulting in the Navier-Stokes equations for each x-, y-, and z- component. The equations are as follows:

$$\rho\frac{Du}{Dt} = \rho g_x - \frac{\partial p}{\partial x} + \frac{\partial}{\partial x}\left[\mu\left(2\frac{\partial u}{\partial x} - \frac{2}{3}\nabla\cdot\vec{V}\right)\right] + \frac{\partial}{\partial y}\left[\mu\left(\frac{\partial u}{\partial y} + \frac{\partial v}{\partial x}\right)\right] + \frac{\partial}{\partial z}\left[\mu\left(\frac{\partial w}{\partial x} + \frac{\partial u}{\partial z}\right)\right] \qquad (2.17)$$

$$\rho\frac{Dv}{Dt} = \rho g_y - \frac{\partial p}{\partial y} + \frac{\partial}{\partial x}\left[\mu\left(\frac{\partial u}{\partial y} + \frac{\partial v}{\partial x}\right)\right] + \frac{\partial}{\partial y}\left[\mu\left(2\frac{\partial v}{\partial y} - \frac{2}{3}\nabla\cdot\vec{V}\right)\right] + \frac{\partial}{\partial z}\left[\mu\left(\frac{\partial v}{\partial z} + \frac{\partial w}{\partial y}\right)\right] \qquad (2.18)$$

$$\rho\frac{Dw}{Dt} = \rho g_z - \frac{\partial p}{\partial z} + \frac{\partial}{\partial x}\left[\mu\left(\frac{\partial w}{\partial x} + \frac{\partial u}{\partial z}\right)\right] + \frac{\partial}{\partial y}\left[\mu\left(\frac{\partial v}{\partial z} + \frac{\partial w}{\partial y}\right)\right] + \frac{\partial}{\partial z}\left[\mu\left(2\frac{\partial w}{\partial z} - \frac{2}{3}\nabla\cdot\vec{V}\right)\right] \qquad (2.19)$$

Above Equations 2.17 – 2.19 can be further reduced when a flow is assumed to be incompressible and has a constant viscosity. These assumptions were the same for flow over the wind deflectors only, rooftop solar panel racks only, and the

combination of racks with wind deflectors. The reduced form, and more recognizable

form of the Navier-Stokes equations, can be found in Equations 2.20 – 2.22.

$$\rho\left(\frac{\partial u}{\partial t} + u\frac{\partial u}{\partial x} + v\frac{\partial u}{\partial y} + w\frac{\partial u}{\partial z}\right) = -\frac{\partial p}{\partial x} + \mu\left(\frac{\partial^2 u}{\partial x^2} + \frac{\partial^2 u}{\partial y^2} + \frac{\partial^2 u}{\partial z^2}\right) + \rho g_x \tag{2.20}$$

$$\rho\left(\frac{\partial v}{\partial t} + u\frac{\partial v}{\partial x} + v\frac{\partial v}{\partial y} + w\frac{\partial v}{\partial z}\right) = -\frac{\partial p}{\partial y} + \mu\left(\frac{\partial^2 v}{\partial x^2} + \frac{\partial^2 v}{\partial y^2} + \frac{\partial^2 v}{\partial z^2}\right) + \rho g_y \tag{2.21}$$

$$\rho\left(\frac{\partial w}{\partial t} + u\frac{\partial w}{\partial x} + v\frac{\partial w}{\partial y} + w\frac{\partial w}{\partial z}\right) = -\frac{\partial p}{\partial z} + \mu\left(\frac{\partial^2 w}{\partial x^2} + \frac{\partial^2 w}{\partial y^2} + \frac{\partial^2 w}{\partial z^2}\right) + \rho g_z \tag{2.22}$$

Taking into account the assumptions stated earlier in this Chapter, the

equations can be reduced further. Also, only two-dimensional flow was considered.

The simplified Navier-Stokes equations are expressed as Equations 2.23 and 2.24.

$$\rho\left(u\frac{\partial u}{\partial x} + v\frac{\partial u}{\partial y} + w\frac{\partial u}{\partial z}\right) = -\frac{\partial p}{\partial x} + \mu\left(\frac{\partial^2 u}{\partial x^2} + \frac{\partial^2 u}{\partial y^2} + \frac{\partial^2 u}{\partial z^2}\right) \tag{2.23}$$

$$\rho\left(u\frac{\partial v}{\partial x} + v\frac{\partial v}{\partial y} + w\frac{\partial v}{\partial z}\right) = -\frac{\partial p}{\partial y} + \mu\left(\frac{\partial^2 v}{\partial x^2} + \frac{\partial^2 v}{\partial y^2} + \frac{\partial^2 v}{\partial z^2}\right) \tag{2.24}$$

In summary, the derivation of governing fluid flow with boundary conditions can

be expressed as follows:

Continuity:

$$\nabla \bullet \mathbf{u} = 0 \tag{2.25}$$

Navier-Stokes equations:

$$\rho\ \mathbf{u} \bullet \nabla \mathbf{u} = -\nabla p + \mu \nabla^2 \mathbf{u} + \mathbf{F}_L \tag{2.26}$$

Where $\rho$ is the fluid density, $\nabla p$ is pressure gradient, $F_L$ ($= J \times B$) is induced

Lorentz force in the RedOx ionic solution and $\mu$ is viscosity of the fluid. Fluid

velocity $\mathbf{u}$ is defined as $\mathbf{u} = u e_x + u e_y + u e_z$, in which u, v, and w represent, respectively,

the velocity components in the x-, y- and z- directions.

Simultaneously solving these two equations with appropriate initial and boundary conditions, general characteristics of fluid flow can be identified. Referring to Figure 2.3, following no-slip boundary conditions for velocities were used in COMSOL 3.5a:

Front side of the microchannel: $\qquad u(x,0,z) = 0$ $\qquad\qquad$ (2.27)

Back side of the microchannel: $\qquad u(x,W,z) = 0$ $\qquad\qquad$ (2.28)

Bottom side of the microchannel: $\qquad u(x,y,0) = 0$ $\qquad\qquad$ (2.29)

Top side of the microchannel: $\qquad u(x,y,H) = 0$ $\qquad\qquad$ (2.30)

In the absence of the pressure gradient along the channel,

$$p(0,y,z) = p \text{ or } 0 \qquad\qquad (2.31)$$

$$p(L,y,z) = p \text{ or } 0, \text{ i.e., } \nabla p = 0 \qquad\qquad (2.32)$$

Similarly, normal pressure boundary conditions were used at the inlet (x=0) and the outlet (x=L) of the microchannel:

$$\mathbf{t.u}(0,y,z)=0 \qquad\qquad (2.33)$$

$$\mathbf{t.u}(L,y,z)=0, \qquad\qquad (2.34)$$

Where $\mathbf{t}$ is the unit vector tangent to the planes at x=0 and x=L.

To numerically solve the flow field using the a set of equations from (2.25) and (2.26) subjected to their boundary conditions (2.27)-(2.34), the spatial distribution of resulting current density $\mathbf{J} = J_x \, \mathbf{e_x} + J_y \, \mathbf{e_y} + J_z \, \mathbf{e_z}$, within the RedOx based ionic solution (Physics of Multi-Ionic Mass Transport) is required, and is followed the next.

### 2.2.2 Physics of Multi-Ionic Mass Transport

We present a multi-ion mass transport model by Nernst-Planck equation for the concentration of each species. It is assumed that there are K dissolved ionic species(here we have three ionic species involved) in the solution.

The flux density due to convection, diffusion, and migration is given by:

$$\mathbf{N}_k = \mathbf{u}\,c_k - D_k \nabla c_k - z_k m_k F c_k \nabla V\,, \quad k=1, \dots, K. \tag{2.35}$$

Where $c_k$ is the molar concentration, $D_k$ is the diffusion coefficient, $z_k$ is the valence of each ionic species, and $m_k$ is the mobility of the $k^{th}$ ionic species. F is Faraday's constant (F=96484.6 C/mol) and V is the electric potential in the solution.

According to Nernst-Einstein expression, the relationship between migration coefficient ($m_k$)and diffusion coefficient ($D_k$) is given by:

$$m_k = \frac{D_k}{RT}\,, \quad k=1, \dots, K, \tag{2.36}$$

Where R is the universal gas constant and T is the absolute temperature of the electrolyte solution.

According to Nernst-Planck expression, the concentration of each ionic species under steady state is governed by:

$$\nabla \bullet \mathbf{N}_k = \frac{\partial N_{kx}}{\partial x} + \frac{\partial N_{ky}}{\partial y} + \frac{\partial N_{kz}}{\partial z} = 0\,, \quad k=1, \dots, K. \tag{2.37}$$

Where, $N_{kx}$, $N_{ky}$, and $N_{kz}$ represent, respectively, the x-, y-, and z- components of the $k^{th}$ species's flux densities.

The local electroneutrality condition for K ionic species in the solution is given by:

$$\sum_{K=1}^{K} z_k c_k = 0 \tag{2.38}$$

Since the width of the microchannel is sufficiently larger than the thickness of the electric double layers formed around the electrode surface walls, electric double layers are not considered in the mathematical modeling of the multi-ion mass transport.

The current density **J** in the RedOx ionic solution due to convection, diffusion, and migration is expressed as:

$$J = F \sum_{k=1}^{k} z_k N_k \tag{2.39}$$

The current density **J** induces due to the interaction between the magnetic field **B** when applied electric potential V across the electrodes. The constitution of the Nernst-Planck equations and the local electroneutrality condition defines an accepted approximation of electrochemical mass transport phenomenon. The boundary condition for each ionic species and the applied electric potential in the RedOx ionic solution is required to be able to numerically simulate the multi-ion mass transport. The net ionic fluxes of the inert species ($K^+$ ions in this case) normal to the walls of the microchannel are zero: for the inert species k on the all solid walls,

$$\mathbf{n} \cdot \mathbf{N_k} = 0 \tag{2.40}$$

Where **n** is the unit vector normal to the solid wall surface.

The concentrations of each other electro-active species normal to the walls where no electrochemical reactions occur are also assumed to be zero: for the electroactive species k on the dielectric walls,

$$\mathbf{n} \cdot \mathbf{N_k} = 0 \tag{2.41}$$

For RedOx couple, the oxidation and reduction reactions occur, respectively, at the surfaces of the anode and cathode:

$$\mathbf{Ox} + ne^- \rightleftharpoons \mathbf{Red} \tag{2.42}$$

When the RedOx ionic species is a mixture of $K_4[Fe(CN)_6]/K_3[Fe(CN)_6]$ ionic solution, **Ox** and **Red** in the above electrochemical reaction correspond, respectively, to $[Fe(CN)_6]^{3-}$ and $[Fe(CN)_6]^{4-}$, and n=1.

$$[Fe(CN)_6]^{3-} + e^- \rightleftharpoons [Fe(CN)_6]^{4-} \tag{2.43}$$

According to the Butler-Volmer equation, the kinetics of the electrodes' reactions is described by the following expression (Newman 1991 and Bard 2000):

$$\mathbf{n \cdot N_{Red}} = - \mathbf{n \cdot N_{Ox}} = k_0 \left( c_{Ox} e^{-\frac{\alpha nF}{RT}\eta} - c_{Red} e^{-\frac{(1-\alpha)nF}{RT}\eta} \right) \tag{2.44}$$

Where $c_{Ox}$ and $c_{Red}$ are the concentrations of the electroactive ionic species that are involved in the electrochemical reaction at the electric double layer; $\alpha$ is the charge transfer coefficient for the cathodic reaction, usually ranging from 0.0 to 1.0 9assumed as 0.5); *n* represents the number of electrons exchanged in the reaction; $k_0$ is the reaction rate constant; and

$$\eta \ \{= \quad \begin{array}{l} (U_{an}\text{-}V), \text{ along the surface of anode} \\ (U_{ca}\text{-}V), \text{ along the surface of cathode} \end{array} \tag{2.45}$$

In the above equation, $U_{an}$ and $U_{ca}$ are, respectively, the imposed potential on the anode and cathode, and $\Delta V = U_{an} - U_{ca}$ represents the potential difference applied to the opposing electrodes.

Boundary conditions used for the multi-ion mass transport are described hereafter.

At the inlet cross-section (x= 0) are given by

$$c_k(0,y,z) = c_{k0}, \quad k=1,...,K, \tag{2.46}$$

and the electroneutrality condition $\sum_{k=1}^{k} z_k c_k = 0$.

Here, $C_{ko}$ is determined from the bulk concentrations in the reservoir. Furthermore, far upstream of the electrodes, the electric field was assumed to be insignificant. At the inlet and exit cross sections of the microchannel, x-component of electric field is assumed to be zero as shown below:

$$\mathbf{n} \cdot \nabla V \,( \, 0 \,, \, y \,, \, z \,) = 0 \tag{2.47}$$

$$\mathbf{n} \cdot \nabla V \,( \, L \,, \, y \,, \, z \,) = 0 \tag{2.48}$$

Along the dielectric walls of the channel, the electric fields normal to the walls are also assumed to be zero as shown below:

$$\mathbf{n} \cdot \nabla V \,( \, x \,, \, y \,, \, z \,) = 0 \tag{2.49}$$

The potentials of the electrolyte adjacent to the electric double layers are different than the applied potentials across the electrodes. There is also a potential drop across the electric double layer. The potentials of the RedOx ionic species next to the electric double layers of both anode and cathode can be computed by using the following expression:

$$\mathbf{n} \bullet \mathbf{J} = nFk_0 \left( c_{Ox} e^{-\frac{\alpha nF}{RT}\eta} - c_{Red} e^{\frac{(1-\alpha)nF}{RT}\eta} \right)$$

$$\tag{2.50}$$

The transport of species at the exit cross-section *(x=L)* is dominated by convection due to sufficiently large Peclet numbers in the MHD flow (Qian et al 2006) in which the diffusion and the migration can be neglected as shown below:

$$\mathbf{n} \cdot \mathbf{N_k} = \mathbf{n} \cdot (c_k u), \quad k=1,...,K, \tag{2.51}$$

The coupled models of fluid flow and the ionic mass transport are so strongly connected that the flow field affects the mass transport due to the convective flux (2.35) and (2.51). This is also true that the mass transport affects the flow field as the current density, $\mathbf{J}$, affects the flow field through the induced Lorentz force $\mathbf{J} \times \mathbf{B}$ and vice versa. This is the reason that this strongly correlated multiphysics phenomenon has to be solved by simultaneously the physics of fluid flow (consisting of continuity and Navier-Stokes equations) and the physics of multi-ion mass transport (consisting of Nernst-Planck equations, the electroneutrality condition, ionic species concentrations, and the potential of the RedOx based solution).

# CHAPTER 3

## NUMERICAL MODELING

Numerical analysis involves simulating fluid flow in the micro-conduits through the use of an algorithm and mathematical model. Numerical simulation and modeling allows for these mathematical equations to be solved. Software that combines numerical techniques with the intricacies of fluid flow is utilized. COMSOL 3.5a allows solving a highly complex fluid flow problem with other multiphysics involved. COMSOL Multiphysics is a powerful interactive environment for modeling and solving all kinds of scientific and engineering problems based on partial differential equations (PDEs). This software can easily extend conventional models for one type of physics into multiphysics models that solve coupled physics phenomena— and do so simultaneously. COMSOL Multiphysics then internally compiles a set of PDEs representing the entire model. The meshing schemes depending on the quality of the mesh, enable to achieve varying degrees of accuracy; the finer the mesh, the more accurate the solution. Due to the nature of the problem and the features, a commercially available finite element software COMSOL was used for simulation. The processing and post-processing of the meshed model were performed in COMSOL.

The algorithms and programs that were used in the study of fluid flow and ionic mass transport are discussed in the sections that follow. COMSOL 3.5a couples the equations of flow theory with mathematical models in order to solve highly complex fluid flows. COMSOL Multiphysics includes a number of different solvers for PDE-based problems. Table 3.1 summarizes the available types.

**Table 3.1.** COMSOL Multiphysics Solver Types and their Usage

| Solver Type | Usage |
|---|---|
| Stationary | For stationary PDE problems (linear or nonlinear) |
| Time-dependent | For time-dependent PDE problems (linear or nonlinear) |
| Eigen value | For eigenvalue PDE problems |
| Parametric | For parameterized sets of stationary PDE problems (linear or nonlinear) |
| Stationary segregated | For stationary multiphysics PDE problems (linear or nonlinear) |
| Parametric segregated | For parameterized sets of stationary multiphysics PDE problems (linear or nonlinear) |
| Adaptive | For stationary (linear or nonlinear) or eigenvalue PDE problems using adaptive mesh refinement |

The **Stationary Segregated** Solver is using to solve the microfluid flow. The solver will be discussed in section **3.2 Multiphysics Solver Techniques**.

## 3.1 Multiphysics Methodology

Computational fluid dynamics(CFD) numerical analysis involving multiphysics requires a construction of finite element grid. The general procedures include geometrical drawing, subdomain setting, boundary set up, meshing, simulation and result post processing. COMSOL 3.5a was used to perform all the required steps from creating models to post processing, Figure 3.1.

**Solid modeling**
- Geometric construction of model
- Defining domain properties

**Pre-processing**
- Meshing of domain
- Setting up of boundary conditions
- Setting up sub-domain

**Processing**
- Setting of solvers
- Simulation of models

**Post-processing**
- Visualization of results
- X,Y plot
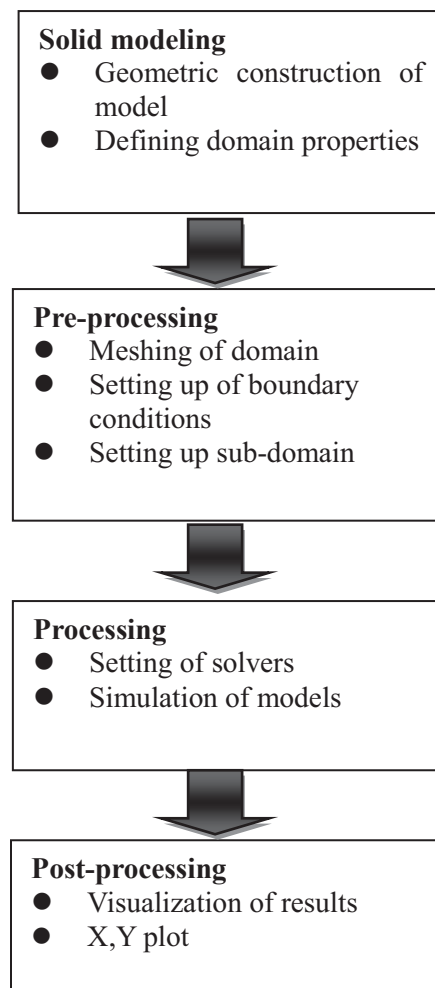
**Figure 3.1.** Basic Program Structure of Numerical Simulation in COMSOL 3.5a

1.    Construction of the geometrical models using COMSOL 3.5a 2D and 3D drawing with two different modules: Nernst-Plank from Chemical Engineering Module for mass transport modeling and Incompressible Navier-Stokes for fluid flow modeling was used.

2.    Division of the fluid domain of the geometrical model into discrete volumes using appropriate meshing parameters. In COMSOL 3.5a, 3D mesh generator was used with tetrahedral, hexahedral, or prism mesh elements whose faces, edges, and corners are called mesh faces, mesh edges, and mesh vertices, respectively. 3D mesh generator includes various shapes of mesh elements. The geometrical boundaries of the model are also automatically partitioned into triangular or quadrilateral boundary elements. The geometric edges are partitioned into edge elements. Isolated geometric vertices become mesh vertices. The free mesher is allows for all types of geometry regardless of the topology and shape of geometry. Boundary conditions define the interface between the model geometry and its surroundings. The subdomain setting describes the physics on a model's main domain, which may be divided into a number of subdomains. The Navier-stokes equations describe laminar flow of viscous fluids through continuity and momentum equations for each respective component of the momentum vector in all spatial dimensions. The Nernst–Planck equation is a conservation of mass equation used to describe the motion of chemical species in a fluid medium. It describes the flux of ions under the influence of both an ionic concentration gradient and an electric field.

3.    Before the simulation is begun, the solver parameters setting must be completed. In analysis type's task, we chose **Stationary** solver for both flow and mass transport physics**.** The linear system solver is chosen as **Direct (PARDISO)** for its highly efficient direct solver for both symmetric and nonsymmetrical systems.

4.      To help you analyze results from its solvers, COMSOL Multiphysics provides numerous postprocessing and visualization tools, including advanced graphics, data display and export functions, and a report generator.

## 3.2  Multiphysics Solver Techniques

The selection of the solver is very important for more accurate results when compared with experimental results and for fewer errors. The user must specify the type of solver, pressure or density based, and whether the flow is steady or unsteady.

The fluid flow was considered as a steady state flow in order to simplify the CFD simulations for the microfluids flow. The stationary  solver will be discussed in the following.

### 3.2.1  Stationary Segregated Algorithm

Use the stationary segregated solver for linear or nonlinear stationary PDE problems to split the solution steps into substeps. Define the different substeps by grouping solution components' names together. In a solution step for a substep, the segregated solver uses the damped Newton method and computes only the Jacobian related to the solution components, a procedure that can save both memory and assembly time. Also, it is possible to choose which linear system solver to use in a substep independently from other substeps. For problems where a full Newton approach does not converge, a segregated solution approach can sometimes work well. On the other hand, in the vicinity of a solution where the Newton approach converges quadratically, the segregated solver approach often converges more slowly.

For the segregated solver there is a possibility to directly—that is, without any regards to the equations—impose a restriction on the degrees of freedoms. To use this feature, edit the value of freedom edit field and enter a space-separated list whose entries alternate between component names (the names of the degrees of freedom) and limiting values, for example c1 0 c2 1e-3. For these pairs, the solution vector is modified after each substep in such a way that

$$U_j = \max(U_j, U^L)$$
(3.1)

Where, $U_j$'s *are* the corresponding degrees if freedoms and $U_L$ denotes the limiting value. Note that if either $U_j$ or $UL$ is complex valued the real part of that quantity is used in the above equation.

### 3.2.2 PARDISO Direct Solver

The parallel sparse direct linear solver PARDISO works on general systems of the form $Ax = b$. In order to improve sequential and parallel sparse numerical factorization performance, the solver algorithms are based on a Level-3 BLAS update, and they exploit pipelining parallelism with a combination of left-looking and right-looking supernode techniques. The code is written in C and Fortran. COMSOL Multiphysics uses the PARDISO version developed by Olaf Schenk and collaborators, which is included with Intel MKL (Intel Math Kernel Library).

In the Linear System Solver Settings dialog box, following preordering algorithms can be chosen:

• Minimum degree

• Nested dissection (the default algorithm)

It can also specify if the solver should use a maximum weight matching strategy by choosing row preordering on (default) or off. For symmetric matrices there is a choice between using 2-by-2 Bunch-Kaufmann pivoting (default) or not. In the case of positive definite matrices, row preordering and 2-by-2 Bunch-Kaufmann pivoting are not needed . The solution time is usually reduced if you deselect these features.

To avoid pivoting, PARDISO uses a pivot perturbation strategy that tests the magnitude of the potential pivot against a constant threshold of

$$\varepsilon = \alpha |PP_{\mathrm{MPS}}D_r A D_c P|_\infty \qquad (3.2)$$

Where $P$ and $PMPS$ are permutation matrices, $Dr$ and $Dc$ are diagonal scaling matrices, and is the infinity norm (maximum norm). If the solver encounters a tiny pivot during elimination, it sets it to

$$\mathrm{sign}(l_{ii})\varepsilon |PP_{\mathrm{MPS}}D_r A D_c P|_\infty \qquad (3.3)$$

The pivot threshold $\varepsilon$ can be specified as required. The perturbation strategy is not as robust as ordinary pivoting. In order to improve the solution PARDISO uses iterative refinements. PARDISO also includes out-of-core capabilities. The PARDISO out-of-core solver stores the LU factors on the hard drive. This minimizes the internal memory usage. The price is longer solution times because it takes longer time to read and write to disk than using the internal memory. You can specify the temporary directory where PARDISO stores the LU factors using the -tmpdir switch; see page 53 of the COMSOL 3.5a Multiphysics Installation and Operations Guide for further details. The LU factors are stored as blocks on the hard drive. The In core memory option controls the maximum amount of internal memory (in megabytes) allowed for the blocks. If a block is too large to

fit into the maximum allowed internal memory you get an out-of-memory error. In that case you must increase the amount of internal memory that you enter in the In core memory edit field. The default value is 512 MB.

COMSOL 3.5a Multiphysics can optionally estimate and check the error after the solution phase. You control this option through the Check tolerances list. For the Automatic selection, error checking is at least done for problems where pivot perturbation or iterative improvement has been used.

### 3.2.3 Convergence Criteria

The segregated solver terminates if a convergence criterion is fulfilled or if the number of segregated iterations exceeds the number in the Maximum number of segregated iterations edit field (in the Stationary page settings). The value in the Tolerance (default $=$ $10-3$) edit field for each group in the General page settings gives the convergence criterion. The segregated-solver iterations stop when for all groups the relative error estimate is smaller than the corresponding tolerance.

When termination of the segregated solver is based on the estimated error, it terminates if, for all the groups $j$, the error estimate is smaller than the corresponding tolerance,

$$\text{err}_{j,k} < \text{tol}_j,$$

(3.4)

Where, the error estimate in segregated iteration $k$ is

$$\text{err}_{j,k} = \max(e^N_{j,k}, e^S_{j,k})$$

(3.5)

The number $\text{tol}_j$ is taken from the Relative tolerance edit field for the corresponding group settings for the Stationary segregated solver on the General page of the Solver Parameters dialog box. Furthermore,

$$e_{j,k}^{N} = \max_{l}(1-\alpha_{l})\left[\frac{1}{N_j}\sum_{i=1}^{N_j}\left(\frac{\left|(\Delta U^{l,j,k})_i\right|}{W^{j}_i}\right)^2\right]^{1/2}$$

(3.6)

This is an estimate of the largest damped Newton error. Here l is taken for all iterations in all substeps solving for the group j, $\alpha l$ is the damping factor, $\Delta U$ $l, j, k$ is the Newton increment vector, and N$j$ is the number of DOFs. The weight factor W$ji$ is described below.

$$e_{j,k}^{S} = \left[\frac{1}{N_j}\sum_{i=1}^{N_j}\left(\frac{\left|(U^{j,k}-U^{j,k-1})_i\right|}{W^{j}_i}\right)^2\right]^{1/2},$$

(3.7)

Where, $e_{j,k}^{S}$ is the relative increment over one complete iteration k. In this expression, U$j,k$ is the segregated solution vector for the group j, and W$ji$ = max(|U$ji$|, S$i$), where S$i$ is a scale factor that the solver determines from the settings in the Scaling of variables area.

The selection in the Matrix symmetry list applies to all the segregated solver groups. For the Automatic choice, the solver can detect and make use of symmetry for the group Jacobian independently of other groups.

The selection in the Linearity list on the Stationary page applies to all the segregated solver groups. This selection is not as important as it is for the standard stationary solver because the stationary segregated solver uses the same iterative procedure both for linear and nonlinear problems and always checks the error criteria. The associated settings do affect which group Jacobians that are reassembled, and an incorrect selection can therefore result in suboptimal convergence.

# CHAPTER 4

# RESULTS AND DISCUSSION

Three rectangular microchannels, namely; straight, converging and diverging, as discussed earlier were simulated using COMSOL Multiphysics finite element software and the results are presented here. Simulation results have demonstrated the MHD pumping in a rectangular straight microchannel with and without RedOx chemical species in the sample solutions. These results were then compared and analyzed with two other rectangular microchannels, namely; converging and diverging. At last, MHD pumping in rectangular microchannels is compared with equivalent pressure driven pumping in microchannels. This comparison validates and proves the effectiveness of MHD pumping in varieties of microchannels including straight, converging and diverging microchannels for a number of fluid motion control applications including pumping, stirring, mixing, and other lab-on-chip processes.

## 4.1 Rectangular Micro Channel

RedOx-based MHD flow in a 3D planar micro conduit of 18mm in length, 330μm in width, and 670μm in depth was simulated in COMSOL3.5a software. Two electrodes were pattered on the entire side walls of the conduit. Mixture of potassium ferrocyanide/potassium ferricyanide ($K_4[Fe(CN)_6]/K_3[Fe(CN)_6]$) is used as a RedOx chemical couple in the sample solution.

The used RedOx electrolyte is in the absence of any supporting electrolyte e.g., sodium chloride. In order to validate the simulation results, the problem set up in COMSOL 3.5a were made same as those used in the experiments (Aguilar et al. 2006). The RedOx electrolyte solution contains three ions including potassium ($K^+$), ferricyanide ($Fe(CN)_6^{3-}$), and ferrocyanide ($Fe(CN)_6^{4-}$) with their chemical species charges + 1, - 3, and - 4, respectively. The diffusion coefficients at room temperature of the ions $K^+$, $Fe(CN)_6^{3-}$, and $Fe(CN)_6^{4-}$ are, respectively (Bortels et al 1997),

$$D_K{}^+ = 1.957 \times 10^{-9}\, m^2/s,$$

$$D_{Fe(CN)_6}{}^{3-} = 0.896 \times 10^{-9}\, m^2/s, \text{ and}$$

$$D_{Fe(CN)_6}{}^{4-} = 0.735 \times 10^{-9}\, m^2/s$$

It has to be noted that the diffusion coefficient of the chemical species is temperature and pressure dependent. For the electrochemical reaction $Fe(CN)_6^{3-} + e^- \rightleftharpoons Fe(CN)_6{}^{4-}$, the reaction rate constant is $k_o \approx 1.0 \times 10^{-3}\, M/s$, and the charge transfer coefficient is $\alpha \approx$ 0.5 (Bortels et al 1997). The diffusion reaction of the potassium ($K^+$), ferricyanide ($Fe(CN)_6^{3-}$), and ferrocyanide ($Fe(CN)_6^{4-}$) RedOx couple are:

$$K_4\,[Fe\,(CN)_6] \rightleftharpoons K^+ + Fe\,(CN)_6{}^{4-} \text{ and,}$$

$$K_3\,[Fe\,(CN)_6] \rightleftharpoons K^+ + Fe\,(CN)_6{}^{3-}$$

Since the potassium ferricyanide and potassium ferrocyanide RedOx couple has a very high reaction rate constant, the results are not significantly sensitive to values of $k_o$ and $\alpha$. Since the RedOx electrolyte is dilute and with a very low concentrations present in the sample solution, the density and viscosity of water ($\rho \sim 1000\,kg/m^3$ and $\mu \sim 10^{-3}\,Pa.s$) are assumed to be same to the RedOx electrolyte.

In all of these computations, the temperature T = 298K, and the bulk concentrations of both the RedOx species $K_4[Fe(CN)_6]$ and $K_3[Fe(CN)_6]$ in the inlet reservoir (i.e. supplied to the inlet) are taken to be equal. No external pressure difference was assumed between the conduit's inlet and exit reservoir (i.e., $P_1 = P_2$, so $\Delta P = 0$). A schematic of the microchannel is as shown above in Figure 2.2 of chapter 2 which is revisited here as shown above in Figure 4.1.

The steady flow field and ionic concentration field at various potential differences ($\Delta V$), RedOx species concentrations ($C_0$), and magnetic flux densities (B) are obtained by simultaneously solving the coupled mathematical model described earlier in modeling the microchannel. Results of numerical computations for rectangular microchannel were simulated using 3D numerical simulations in COMSOL 3.5a which are experimentally validated (Aguilar et al. 2006). In addition, the simulation results were later compared with the published data (Kabbani et al 2007) and obtained in a close agreement.
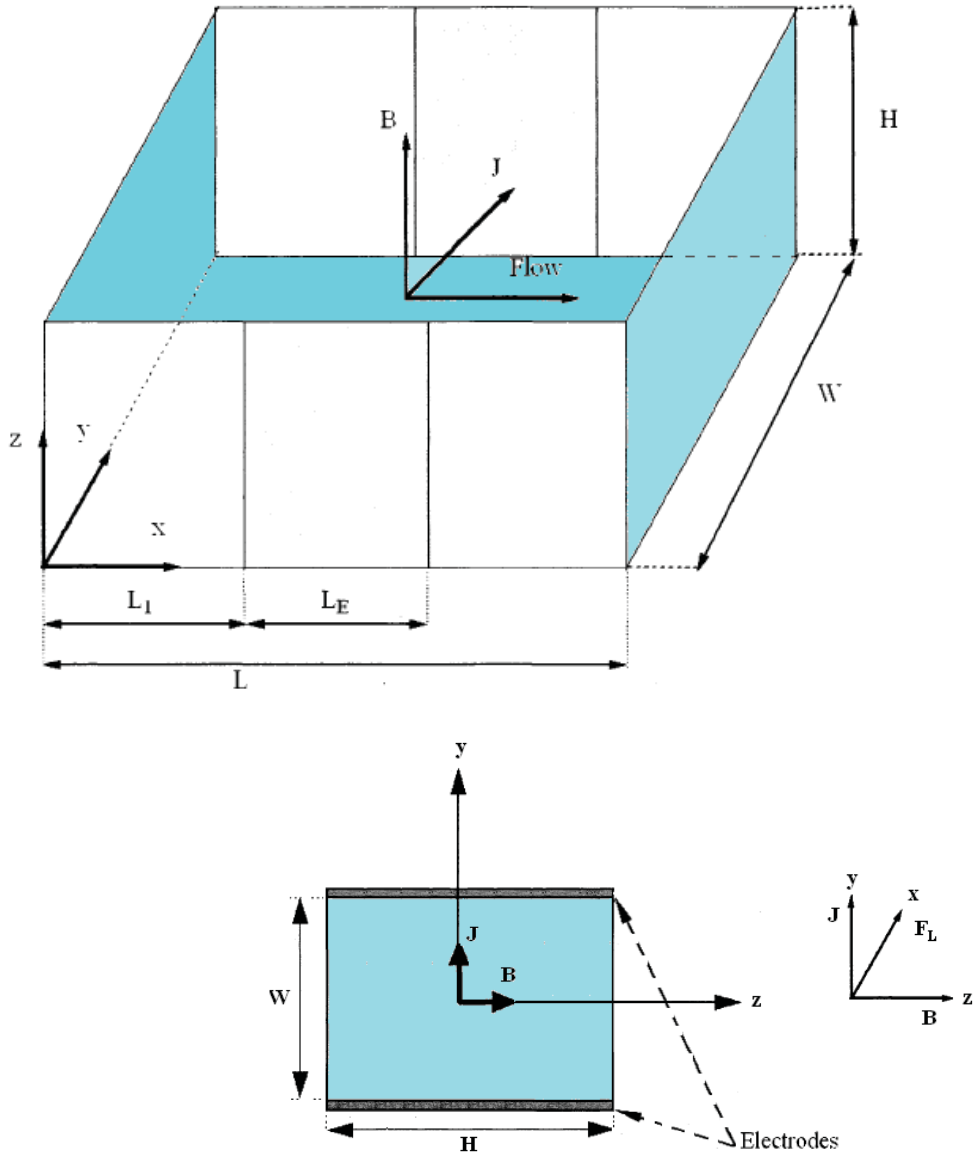
**Figure 4.1.** Schematics of a three-dimensional, planar microchannel patterned with two electrodes along the opposite walls of the microchannel conduit. The conduit is filled with a dilute RedOx chemical species $K_4[Fe(CN)_6]$) and $K_3[Fe(CN)_6]$ which is subjected to a uniform magnetic field of flux density B. A potential difference $\Delta V$ is imposed across the electrodes resulting in a current density J which then oriented orthogonally with the magnetic field to induce the Lorentz forces. The Lorentz forces pump the ionic fluid from the inlet reservoir to the outlet reservoir through the conduit length.

As shown below, Figure 4.2 depicts the steady state current transmitted through

the electrolyte solution as a function of $\Delta V$, the imposed potential difference across the

electrodes in the absence of magnetic field (B) (solid red line) and presence of magnetic field (B) (dashed blue line) when the inlet bulk concentrations of $K_4[Fe(CN)_6]$) and $K_3[Fe(CN)_6]$) are $C_0 = 0.25M$. Resulting current due to the effects of magnetic field is studied without magnetic flux density (i.e., B=0) and with magnetic flux density (i.e., B=0.44T) under a range of different potential differences 0 V to 0.3 V. Representation by the circles (●) and the triangles (▲) are, respectively, for the experimental data obtained from Aguilar et al. (2006) when the magnetic flux densities were B=0 and B=0.44 T. The lines represent the current predictions made by 3D numerical simulations at B = 0 and B = 0.44 T assuming microchannel height and width H>>W as shown in Figure 4.2.

The discrepancies between the numerical predictions and the experimental data may be due to the differences between the actual and assumed diffusion coefficients of the electro active species (Afonien, 2007). When the applied potential difference is low, the resulting current nonlinearly increases with the applied potential difference. Once the potential difference exceeds a certain value, the current reaches the limiting current, and does not increase with the potential difference, thus appears like a plateau. Simulations were not done beyond the applied voltage of 0.30 V.
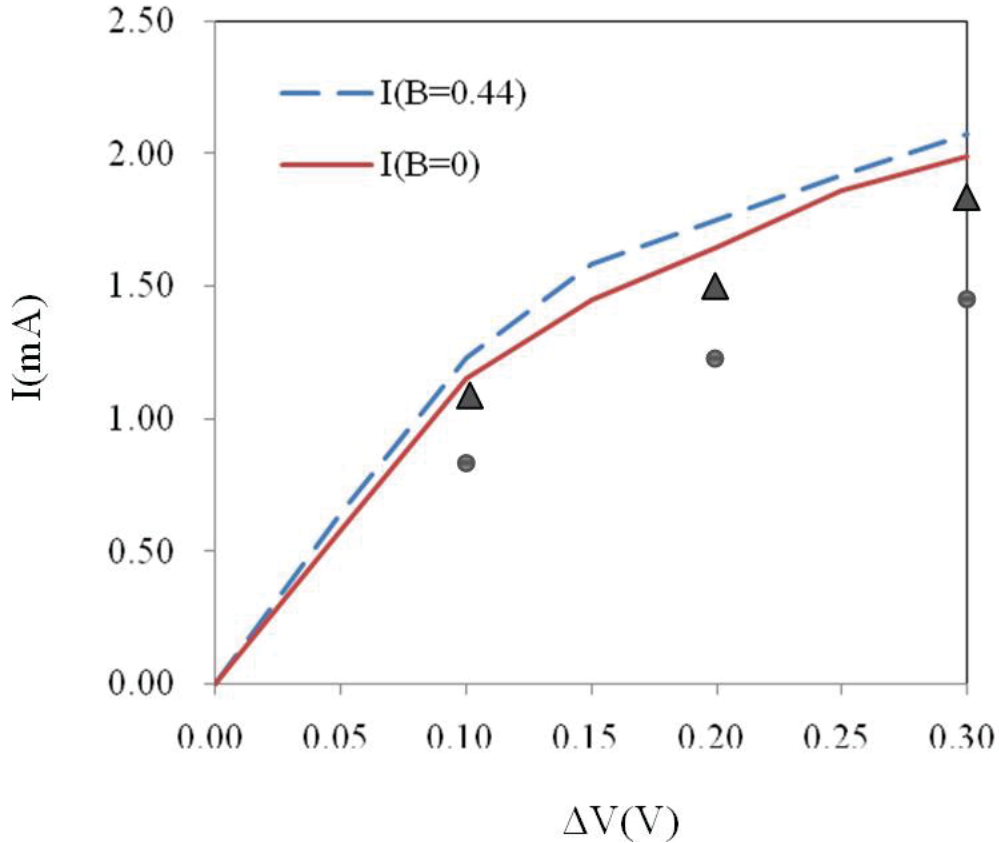
**Figure 4.2.** Effect of applied potential difference on the resulting current in the presence (B=0.44T) and the absence (B=0) of a magnetic field. The circles (●) and triangles (▲) represent, respectively, the experimental data obtained from Aguilar et al. (2006) for the magnetic flux densities of B=0 and B=0.44 T. The solid and the dashed lines represent, respectively, the resulting currents from the 3D model for the magnetic flux densities of B=0 and B=0.44 T. The concentration of the RedOx species ($K_4[Fe(CN)_6]$) /$K_3[Fe(CN)_6]$) C0=0.25 M and the dimensions of the conduit are L=18 mm, W=330 μm and H=670 μm.

In the presence of a magnetic field, induced Lorentz force due to the interaction between the current density and the magnetic field pumps the fluid from the inlet reservoir (at x=0) to the outlet reservoir (at x=L) of the microchannel. The induced fluid motion decreases the boundary layer thickness of the electroactive species concentration next to the electrodes surfaces. This, ultimately, increases the concentration gradient of each species and hence the current density along the electrodes' surfaces. This is the reason to achieve higher total current with magnetohydrodynamic compared to the

absence of a magnetic field where there is no fluid motion in the channel. The 2D approximation is acceptable only when the aspect ratio of the channel H/W>>1 as the 3D effects of z-boundaries are neglected for the fluid motion and hence the respective ionic mass transport. For the aspect ratio H/W≥2, results obtained from 3D simulations are closer to the experimental data as it also captures the 3D effects.

RedOx MHD flow can also be approximated with a fully developed duct flow with a rectangular cross-section which follows the similar procedure as the MHD flow in the absence of the RedOx chemical species. Approximation of the velocity profile and the estimation of the average velocity can be made by the following Equations (4.1) and (4.7) (Juan, 2007 and Kabbani, 2008) as shown below the closed form expressions.

In most regions of the planar microchannel, the current density J is directed nearly normal to the opposite electrodes' surfaces, and the induced Lorentz force J×B is thus directed along the x direction towards outlet. Consequently, the velocity components in the y and z directions are at least two orders of magnitude lower than the velocity component in the x direction. The x component velocity is nearly independent of the coordinate x. Since the induced Lorentz force is a body force, the induced MHD flow is equivalent to a fully developed pressure-driven flow in a three-dimensional microchannel. The x-component velocity can be approximated with that of a fully developed duct flow with a rectangular cross section (White, 2006):

$$u(y,z) = A \sum_{i=1,3,5,\ldots}^{\infty} (-1)^{\frac{i-1}{2}} \left[ 1 - \frac{\cosh\left(\frac{i\pi(z-b)}{2a}\right)}{\cosh\left(\frac{i\pi b}{2a}\right)} \right] \frac{\cos\left(\frac{i\pi(y-a)}{2a}\right)}{i^3}$$

(4.1)

Where, A is the area of the cross-section in the y-z plane of the channel.

45

$a=W/2$, and $b=H/2$

$$A = \frac{48\bar{U}}{\pi^3 \left[ 1 - \frac{192a}{\pi^5 b} \sum_{j=1,3,5,\ldots}^{\infty} \frac{\tanh(j\pi b / 2a)}{j^5} \right]}$$

(4.2)

The velocity profile can be approximated with the following closed form approximation with an error less than 1% (Natarajan and Lakshmanan, 1972):

$$u(y,z) = \bar{U} \left( \frac{m+1}{m} \right) \left( \frac{n+1}{n} \right) \left[ 1 - \left( \frac{|y-a|}{a} \right)^n \right] \left[ 1 - \left( \frac{|z-b|}{b} \right)^m \right]$$

(4.3)

With,

$$m = 1.7 + 0.5 \left( \frac{b}{a} \right)^{-1.4} \quad \text{and} \quad n = \begin{cases} 2 & \text{for } \dfrac{b}{a} \leq \dfrac{1}{3} \\ 2 + 0.3 \left( \dfrac{b}{a} - \dfrac{1}{3} \right) & \text{for } \dfrac{b}{a} \geq \dfrac{1}{3} \end{cases}$$

(4.4)

The steady x-component momentum equation can be approximated by

$$-\frac{\partial p}{\partial x} + \mu \left( \frac{\partial^2 u}{\partial y^2} + \frac{\partial^2 u}{\partial z^2} \right) + J_y B = 0$$

(4.5)

This Navier-Stoke equation represents a relationship between the pressure force, the viscous force and the Lorentz force. Substituting u into this equation, and taking volume integration, average velocity becomes

$$\bar{U} = \frac{BIH - (P_2 - P_1)H^2}{4\mu L \left[ (n+1)\dfrac{H^2}{W^2} + (m+1) \right]}$$

(4.6)

In the absence of the pressure difference between the conduit's inlet and outlet, the average velocity becomes

$$\bar{U} = \frac{BIH}{4\mu L\left[(n+1)\dfrac{H^2}{W^2}+(m+1)\right]}$$

(4.7)

Since the cross-section area of the channel in y-z plane is given by A= W.H. First of all, the optimal height of the channel can be obtained using Equation (4.7) from $d\bar{U}/dH=0$ that gives an expression as shown below:

$$1.5H^6/A^3 +5.7H^4/A^2 -1.9A^{14}/H^{28} - 2.7 = 0$$

(4.8)

The optimal width of the channel can then be calculate by W=A/H from the Equation (4.8). Similarly, the flow rate can be calculated by:

$$Q=\bar{U} A$$

(4.9)

The flow vs. the height of the microchannel for the magnetic flux density B =0.44 T (Afonien, 2007) determined that the optimal height of the microchannel ≈400 μm for the optimal flow rate of 0.15 μl/s. Then the width of the channel was calculated for an assumed cross section area A of the channel by W=A/H, where H≈400 μm.

Without solving the continuity and the Navier-Stokes equations, one can easily solve the coupled mathematical model with the help of the predefined velocity profile (4.3). In order to determine the concentration of each chemical species and the current field, one has to solve the chemical mass transport equations for the 3D approximation model. The total current, I, can be determined by integrating the current density along the positive electrode surface (i.e. anode). The average velocity and the profile of the velocity can be further determined using the expressions (4.3 ) and (4.7 ), respectively.
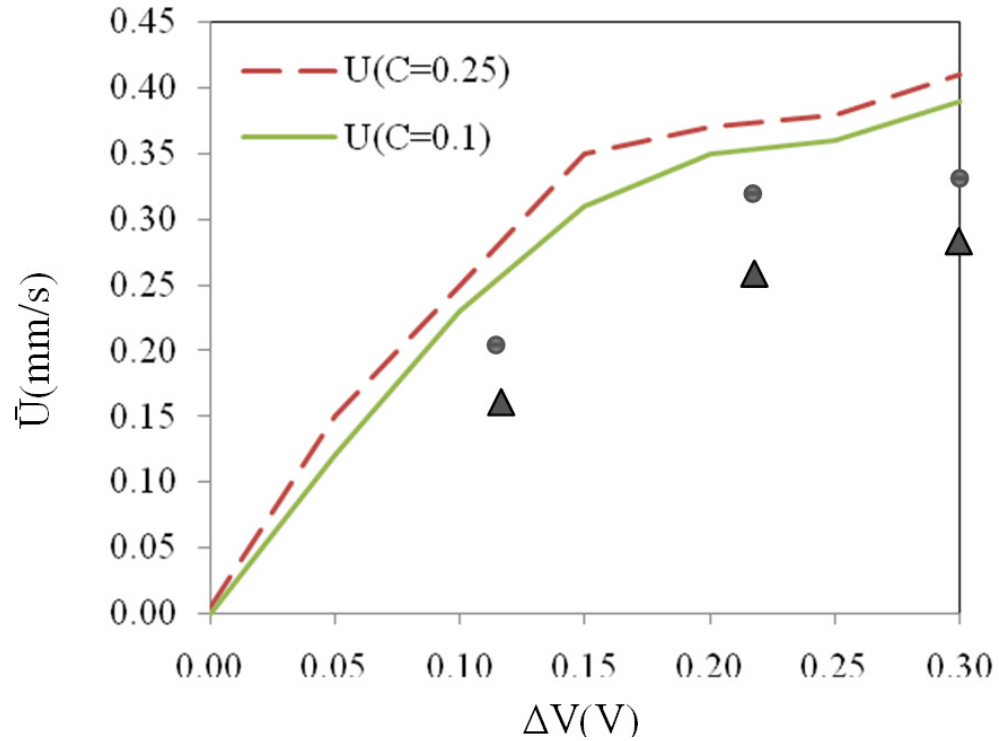
**Figure 4.3.** Effect of potential difference on the average velocity with various concentration of RedOx species $K_4[Fe(CN)_6]$) /$K_3[Fe(CN)_6]$ Co=0.1 M and Co=0.25 M when B=0.44 T. The triangles (▲) and circles (●) represent the experimental data (*Aguilar et al. 2006*) where the solid and the dashed lines represent, respectively, the results obtained from the 3D model simulations. All other conditions are maintained same as of Figure 4.2.

The average velocities obtained from the 3D model and experimental data taken from the literature were compared and validated as shown in Figure 4.3 above. This shows the average velocity, $\bar{U}$, as a function of the applied potential difference, $\Delta V$, for the used bulk concentrations of the RedOx electrolyte for various simulations when the magnetic field B=0.44 T. Figure 4.3 depicts the result of average velocities obtained from 3D model simulation with different RedOx couple concentration C=0.1 M and C=0.25 M.

The data obtained from the full 3D mathematical and the experimental data are obtained in a good agreement. The average velocity increases nonlinearly with the potential difference. This nature is attributed to the nonlinear relationship between the current and the applied potential difference as depicted in Figure 4.3. This is due to the reason that the average velocity is proportional to the current and the average velocity is also directly proportional to the current. In order to maximize the flow rate, it is desirable to apply a potential difference close to the critical value. The critical value in the RedOx-based MHD device is far below the threshold value for water electrolysis; therefore, there is no bubble formation in the RedOx-based MHD device even under DC electric field. The model predictions are over the experimental data in higher concentrations of RedOx chemical species. An experiment can be designed to trace a dye from one end of the channel (at x=0) to the other end (at x=L) during a certain small interval of time Δt from which the average velocity can be estimated as the ratio L/Δt. The measured velocity is appeared to be slower than they really are because the dye can be seen on the exit reservoir only when its concentration got high enough. This is due to the reason of the actual chemical reaction constant of the chemical species and the assumed values for these constants for the COMSOL 3.5a simulation.

Since the average velocity or flow rate is proportional to the resulting current, the average velocity or flow rate reaches the maximum under the limiting current condition under which the concentrations of the Oxidized ions at the surface of the cathode and the Reduced ions at the surface of the anode equal zero, and the resulting current does not change with the externally applied voltage. Figure 4.4 depicts the maximum velocity corresponding to the limiting current condition as a function of the bulk concentration of

the RedOx species. The lines and symbols in Figure 4.4 represent, respectively, the predictions obtained from the 3D numerical simulations and from the closed form approximation using the obtained resulting current as depicted. Maximum velocity corresponding to the average velocity of fluid pumping from the outlet is seen to be increasing with the increment in the concentration of the RedOx species for each of the magnetic field as shown in the Figure 4.4. This is due to the reason that increment in the concentration of RedOx species increases the fluid convection in the fluid motion which eventually causes to increase the total flux density of the ionic fluid in the channel leading to the increase of body force ($F_L = J \times B$) and the fluid pumping as the current density (J) enhances with the increase in total flux density ($N_k$). Thus induced Lorentz force drives the fluid from the inlet to the outlet via microconduit where the electrodes are patterned across the opposite walls and an external magnetic field is positioned making the magnetic field orthogonal with the electric field applied. We should note that the maximum velocity is directly proportional with the average velocity coming out from the outlet of the microchannel. Almost linear increasing relationship in fluid velocity vs. concentration of the RedOx species is observed for the magnetic fields of B = 0.2 T, 0.44 T, 0.6 T and 0.8 T. For higher RedOx concentrations, fluid velocity increases faster compared to the lower concentrations of the RedOx species. This has also been explained in the closed form expression of the fluid velocity and its relationship with the concentration gradient of the RedOx species as developed earlier in the previous chapter.
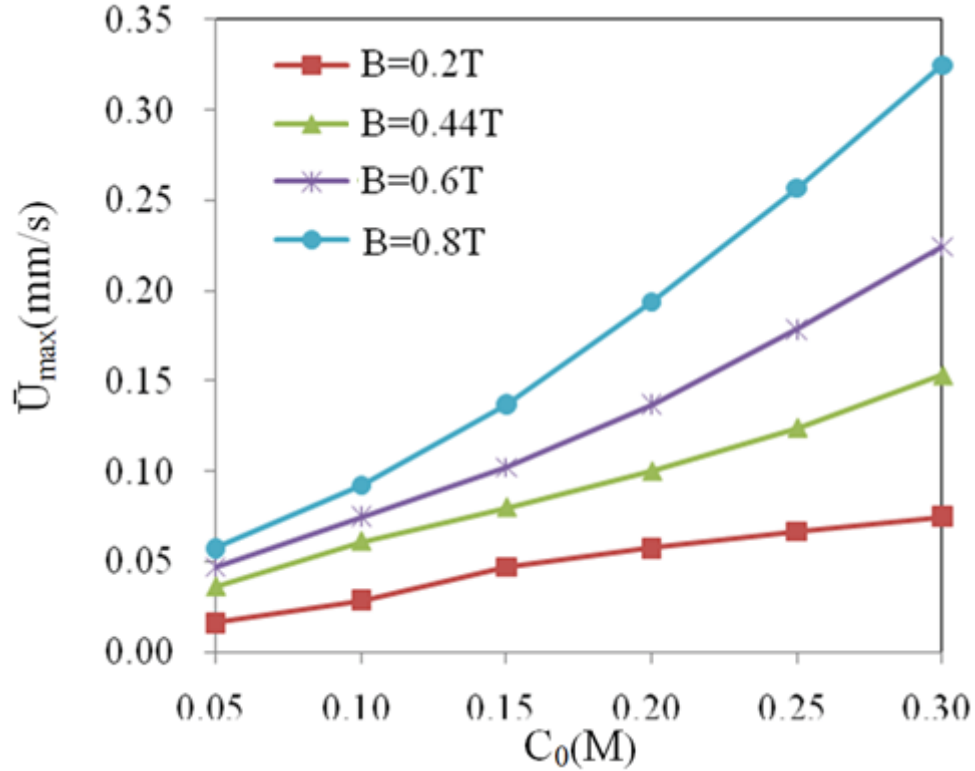
**Figure 4.4.** Effect of RedOx concentration on the maximum velocity with various magnetic flux densities B = 0.2 T, 0.44 T, 0.6 T and 0.8 T for the varying concentration of RedOx species $K_4[Fe(CN)_6])$ /$K_3[Fe(CN)_6]$ Co=0.05 M to 0.30 M . The symbols represent the 3D approximations and the lines represent the results obtained from the 3D model simulations. All other conditions are maintained same as of Figure 4.2.

Finally, Figure 4.5 depicts the maximum velocity corresponding to the limiting current condition as a function of the magnetic flux density under various concentrations of the RedOx species. According to the expression, the effect of the magnetic flux density on the average velocity is due to the combined effects of B on the current and B itself. For low concentration of the species, since the effect of the magnetic flux density on the limiting current is insignificant, the average velocity under the limiting current condition linearly increases as the magnetic flux density increases. The trend of increasing fluid velocity with the higher RedOx concentrations for external magnetic field at B = 0.2 T, 0.3 T, 0.4 T, 0.5 T, 0.6 T and 0.7 T (Figure 4.4) is alike with the increasing trend of fluid

velocity while increasing magnetic flux density for RedOx concentrations at $C_o = 0.05$ M, 0.10 M, 0.15 M, 0.20 M, 0.25 M and 0.30 M (Figure 4.3).
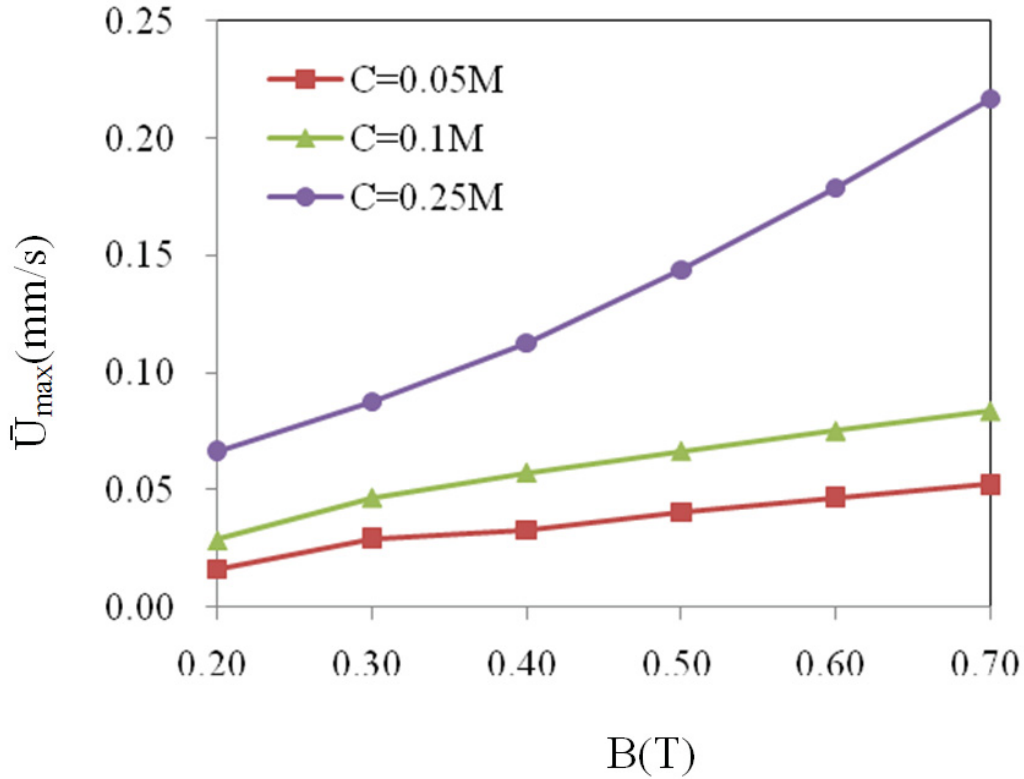


**Figure 4.5.** Effect of magnetic Field on the maximum velocity with various concentration of RedOx species $K_4[Fe(CN)_6])$ $/K_3[Fe(CN)_6]$ Co=0.05M to 0.25M when the magnetic flux densities B = 0.2 T, 0.3 T, 0.4 T, 0.5 T,  0.6 T and 0.7 T. The symbols represent the 3D approximations and the lines represent the results obtained from the 3D model simulations. All other conditions are maintained same as of Figure 4.2.

## 4.2. Comparison of Diverging and Converging Microchannels with Straight Microchannel

For the first part, we have discussed the cross dependencies and effects of various electrical, chemical and magnetic field parameters on fluid motion or pumping of MHD driven fluid flow in a straight microchannel. The parameters include various electric current, and potential difference applied across the electrodes, RedOx chemical species

concentrations, and various magnetic flux densities. Results show the dependencies of outlet fluid velocity on the above mentioned electrical, magnetic and chemical parameters. One can optimize either electrical, or, chemical, or, magnetic field parameters in order to achieve a desired fluid velocity i.e., the flow rate of the fluid from the outlet of the microchannel. There can be a number of other possibilities and opportunities to enhance the desired flow rate from the microchannel outlet by a combinatorial optimization of two or more than two parameters from electrical, or, chemical, or, magnetic field (not performed here).

For the second part, two microchannels, one diverging and other converging shapes were modeled to measure the effectiveness of MHD in various microchannels that also serve to compare their results with the straight microchannel. In the first study, inlet cross sections of all the microchannels were maintained the same but the outlet cross sections were varied. Assuming the straight microchannel as a control model, outlets of the diverging and converging microchannels were made, respectively, double and half the height of the straight microchannel outlet. By doubling the outlet height of the straight microchannel, the outlet cross section of the diverging microchannel becomes twice the outlet cross section of the straight microchannel (*Figures are shown later with the results of velocity vectors).* By halving the outlet height of the straight microchannel, the outlet cross section of the converging microchannel becomes half the outlet cross section of the straight microchannel. Similarly, in the second study, outlet cross sections of all the microchannels were maintained the same but the inlet cross sections were varied which means the inlets of the diverging and converging microchannels were made, respectively, double and half the height of inlet of the straight microchannel *(Figures are shown later*

53

*with the results of velocity vectors).*

### 4.2.1    Velocity Vectors and Velocity Contours

In order to visualize and analyze the action of MHD effects in fluid pumping, the fluid velocity in the microchannel was visualized at inlet ($x \approx 0$), mid-section($x \approx 9$ mm) and outlet ($x \approx 18$ mm) of each micro-conduit. The results show the progression of the fluid pumping from the inlet to the outlet in each microchannel due to the MHD effects by the induced Lorentz force as explained earlier.

### a.  Straight Microchannel

The velocity profiles showing the velocity vectors and the slice contours demonstrate the fluid pumping gradually increasing and the fluid flow profile is becoming stable at the outlet. As shown in the Figure 4.6, the fluid velocity profile is parabolic and becomes maximum at the center axis. As shown in the appendix, the velocity vectors of the fluid in the straight microchannel are shown with the contours of the RedOx concentrations. Since the cross sections of the inlet, mid-section and the outlet are unchanged, MHD driven fluid motion is becoming fully developed as it progresses from the inlet to the outlet due to the fluid convection.
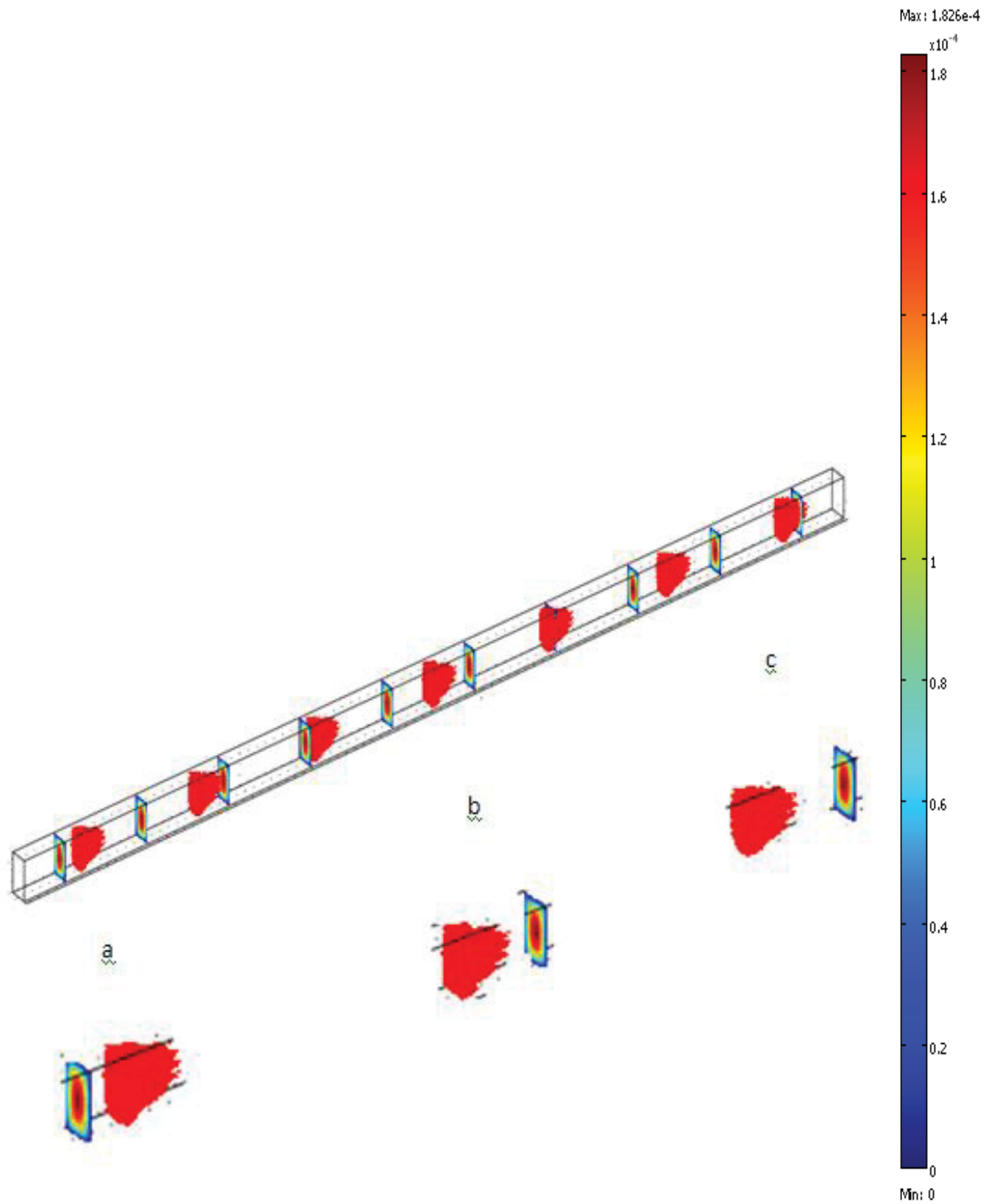
**Figure 4.6.** Velocity Distribution of MHD Fluid Flow in Straight Microchannel with the velocity vectors showing the velocity contours at (a) inlet (b) mid-section and (c) outlet respectively. The concentration of the RedOx species ($K_4[Fe(CN)_6]$) /$K_3[Fe(CN)_6]$) C0=0.25 M when the magnetic flux density, B =0.44 T and the dimensions of the conduit are L=18 mm, W=330 μm and H=670 μm.

Later in this chapter, the MHD driven flow is compared with the equivalent pressure driven flow for the same microchannel without the use of external magnet. This will demonstrate the effectiveness and the promise of the MHD effect in order to levitate the fluid motion in the microchannel for a wide range of applications.

### b. Diverging Microchannel

The velocity profiles showing the velocity vectors and the slice contours demonstrate the fluid pumping gradually increasing and the fluid flow profile is becoming stable at the outlet. As shown in the Figure 4.7, the fluid velocity profile is parabolic and becomes maximum at the center axis. As shown in the appendix, the velocity vectors of the fluid in the diverging microchannel are shown with the contours of the RedOx concentrations. Since the cross sections of the inlet, mid-section and the outlet are varying i.e., the height of the microchannel is gradually increasing as it runs from the inlet to the outlet. MHD driven fluid motion is somewhat becoming fully developed as it progresses from the inlet to the outlet due to the fluid convection. The outlet velocity of the diverging microchannel (135 µm/s) is lower than the outlet velocity of the straight microchannel (160 µm/s). This is due to the reason that outlet cross sectional area of the  diverging microchannel is greater than the outlet cross sectional area of the  straight microchannel. Later in this chapter, the MHD driven flow is compared with the equivalent pressure driven flow for the same microchannel without the use of external magnet. This will demonstrate the effectiveness and the promise of the MHD effect in order to levitate the fluid motion in the microchannel for a wide range of applications.
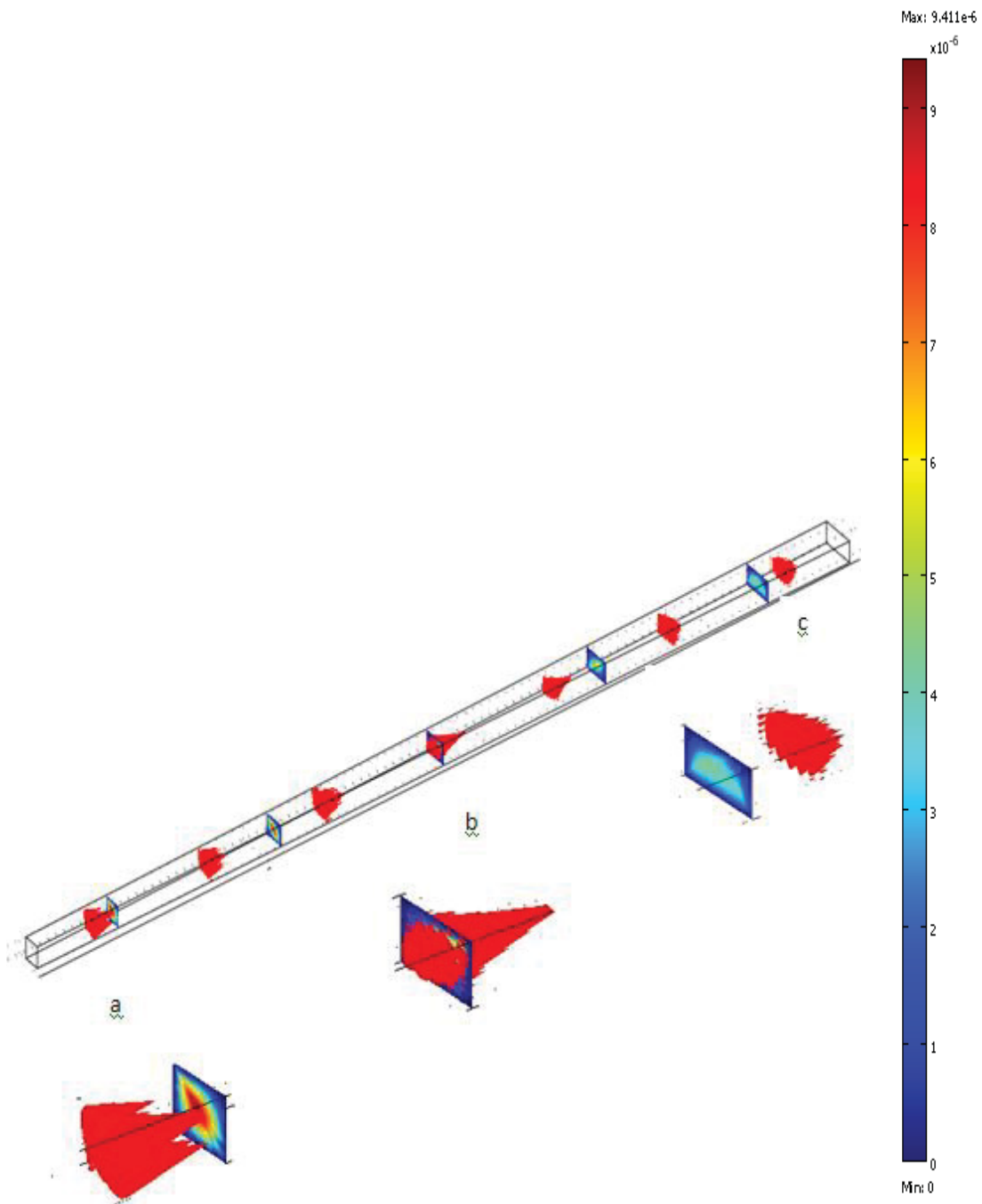
**Figure 4.7.** Velocity Distribution of MHD Fluid Flow in Diverging Microchannel with the velocity vectors showing the velocity contours at (a) inlet (b) mid-section and (c) outlet respectively. The concentration of the RedOx species ($K_4[Fe(CN)_6]$) /$K_3[Fe(CN)_6]$) C0=0.25 M when the magnetic flux density, B =0.44 T and the =dimensions of the conduit are L=18 mm, W=330 μm, inlet H=670 μm and outlet H=1340 μm.

### c. Converging Microchannel

The velocity profiles showing the velocity vectors and the slice contours demonstrate the fluid pumping gradually increasing and the fluid flow profile is becoming stable at the outlet. As shown in the Figure 4.8, the fluid velocity profile is parabolic and becomes maximum at the center axis. As shown in the appendix, the velocity vectors of the fluid in the converging microchannel are shown with the contours of the RedOx concentrations. Since the cross sections of the inlet, mid-section and the outlet are varying i.e., the height of the microchannel is gradually decreasing as it runs from the inlet to the outlet. MHD driven fluid motion is becoming fully developed as it progresses from the inlet to the outlet due to the fluid convection. The outlet velocity of the converging microchannel (260 μm/s) is almost half of the outlet velocity of the straight microchannel (160 μm/s). This is due to the reason that outlet cross sectional area of the converging microchannel is half the outlet cross sectional area of the straight micro channel. Later in this chapter, the MHD driven flow is compared with the equivalent pressure driven flow for the same microchannel without the use of external magnet. This will demonstrate the effectiveness and the promise of the MHD effect in order to levitate the fluid motion in the microchannel for a wide range of applications.
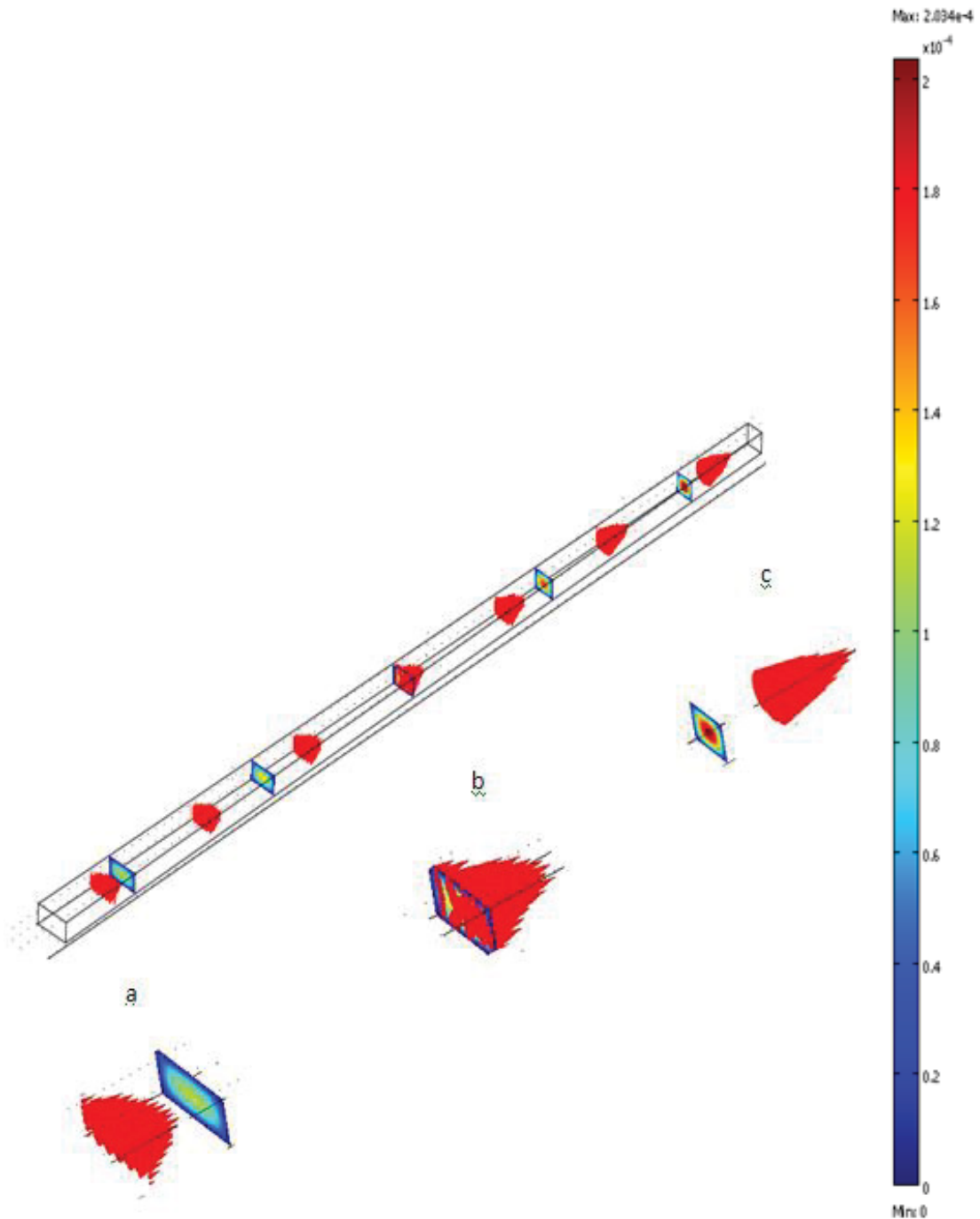
**Figure 4.8.** Velocity Distribution of MHD Fluid Flow in Converging Microchannel with the velocity vectors showing the velocity contours at (a) inlet (b) mid-section and (c) outlet respectively. The concentration of the RedOx species ($K_4[Fe(CN)_6]$) /$K_3[Fe(CN)_6]$) $C_0$=0.25 M when the magnetic flux density, B =0.44 T and the =dimensions of the conduit are L=18 mm, W=330 μm, inlet H=670 μm and outlet H=335 μm.

### 4.2.2 Concentration of Ionic Species ($K^+$, $Fe(CN)_6^{3-}$, and $Fe(CN)_6^{4-}$ )

For all the ionic species involved in the fluid motion, a separate concentration profile was shown in the following Figures 4.4**.,** for **$K^+$, $Fe(CN)_6^{3-}$, and $Fe(CN)_6^{4-}$** ions in three different types of microchannels. In all the microchannels, it has been observed that the **$K^+$** ions are distributed highest to the negative electrode surface and lowest to the positive electrode surface of the microchannel wall. Similarly, **$Fe(CN)_6^{3-}$, and $Fe(CN)_6^{4-}$** RedOx species are distributed highest to the positive electrode surface and lowest to the negative electrode surface of the microchannel wall. When the potential difference is applied across the electrodes, current transmits in the solution that dissociates the three ions **$K^+$, $Fe(CN)_6^{3-}$, and $Fe(CN)_6^{4-}$** which will then be migrated to their respective counter ionic electrodes. These ionic distribution counters verify the migration of ions or the mobility of ions in the solution for the total ionic flux density which is responsible for the induced Lorentz force leading to the fluid pumping.

Figure 4.9 to Figure 4.11 show the concentrations of each chemical species ($K^+$ ,$Fe(CN)_6^{3-}$,and $Fe(CN)_6^{4-}$ ) follow the flow in the subdomain of both diverging and converging channels. Application of potential difference across the walls in each channel, mobility of ions is mainly due to diffusion, convection, and migration leading to the fluid motion from the inlet reservoir to the outlet reservoir.
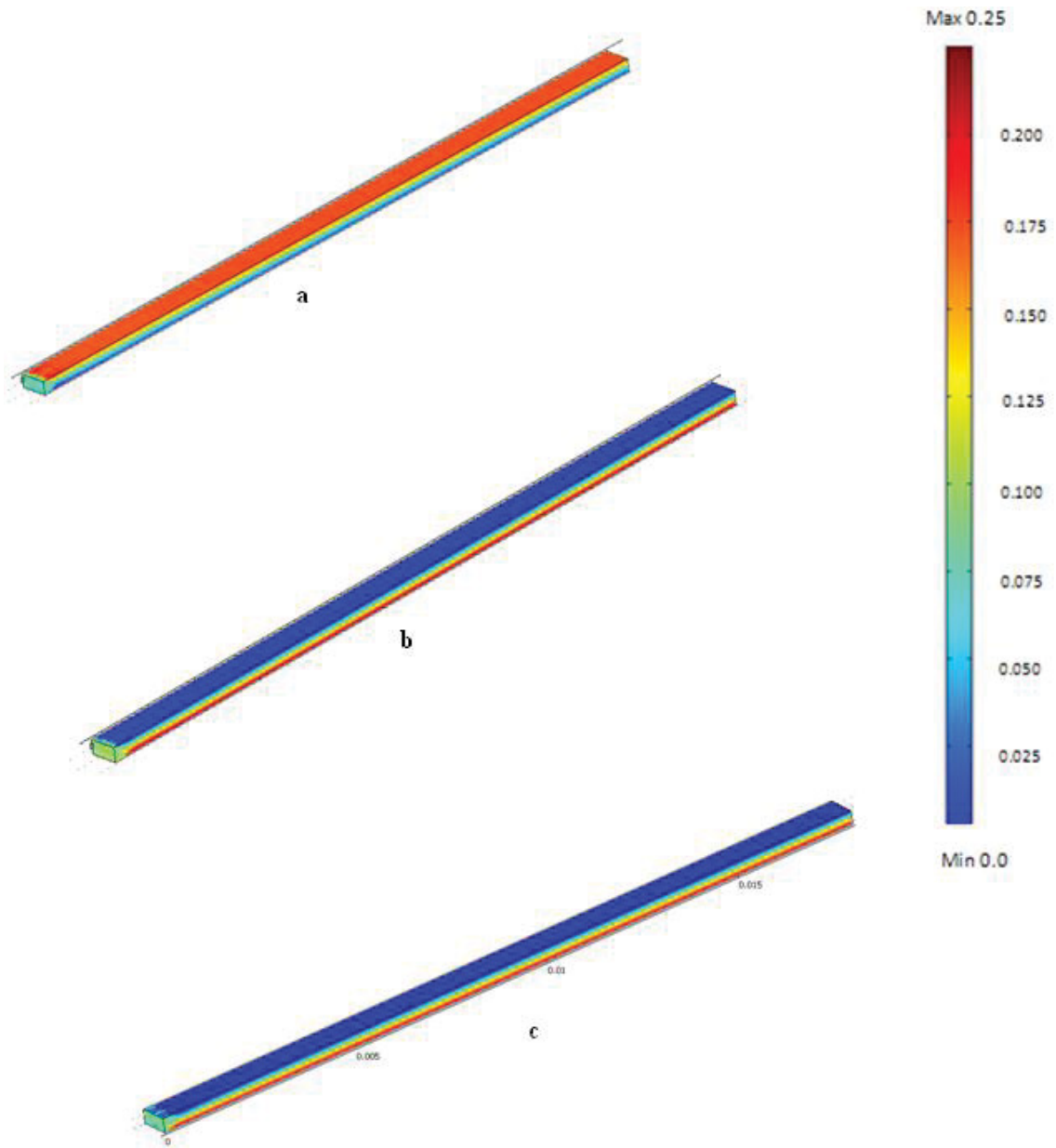
**Figure 4.9.** Concentration Distributions of Ionic Species (a) K+, (b) Fe(CN)$_6^{3-}$ (c) Fe(CN)$_6^{4-}$ in a Straight Microchannel. The concentration of the RedOx species (K$_4$[Fe(CN)$_6$]) /K$_3$[Fe(CN)$_6$]) C0=0.25 M when the magnetic flux density, B =0.44 T and the dimensions of the conduit are L=18 mm, W=330 μm and H=670 μm.
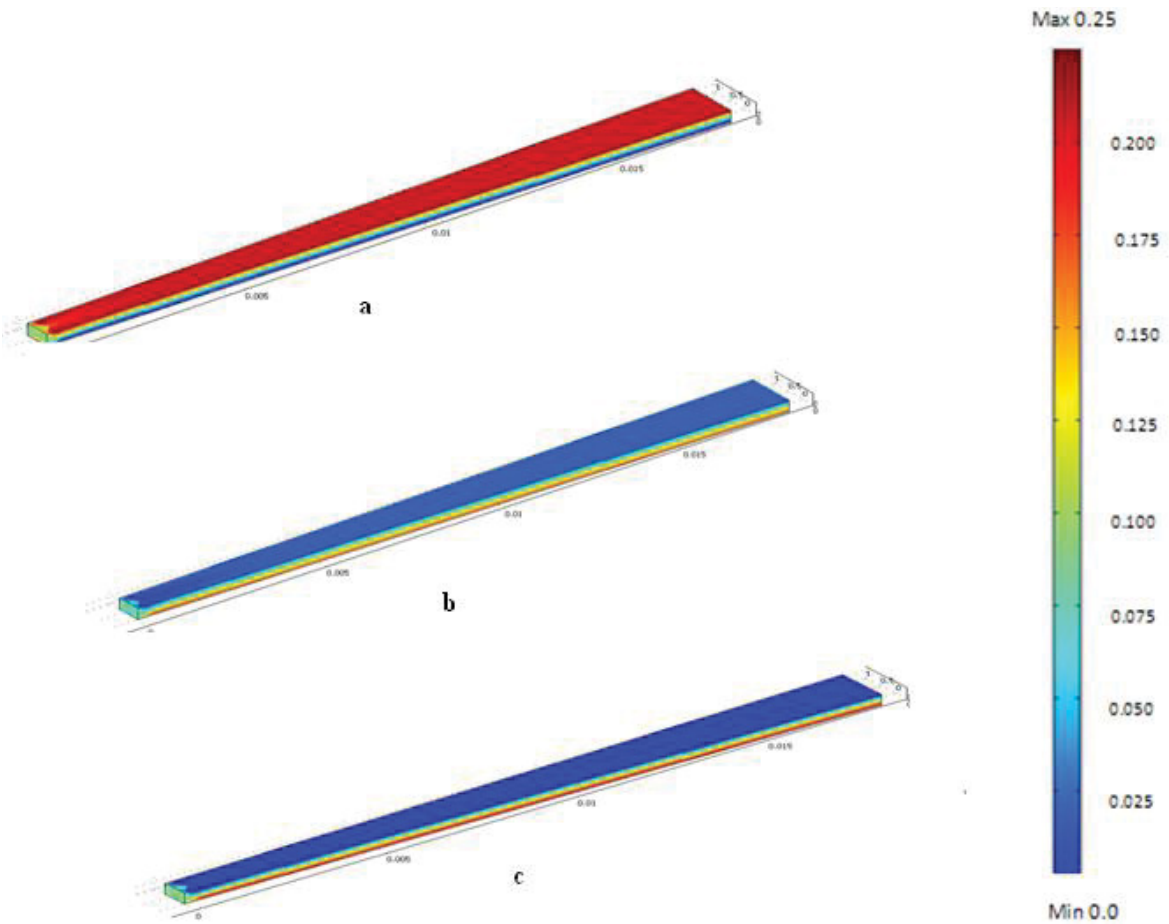
**Figure 4.10.** Concentration Distributions of Ionic Species (a) K+, (b) $Fe(CN)_6^{3-}$ (c) $Fe(CN)_6^{4-}$ in a Diverging Microchannel. The concentration of the RedOx species $(K_4[Fe(CN)_6])$ /$K_3[Fe(CN)_6]$) C0=0.25 M when the magnetic flux density, B =0.44 T and the dimensions of the conduit are L=18 mm, W=330 μm and H=1340 μm.
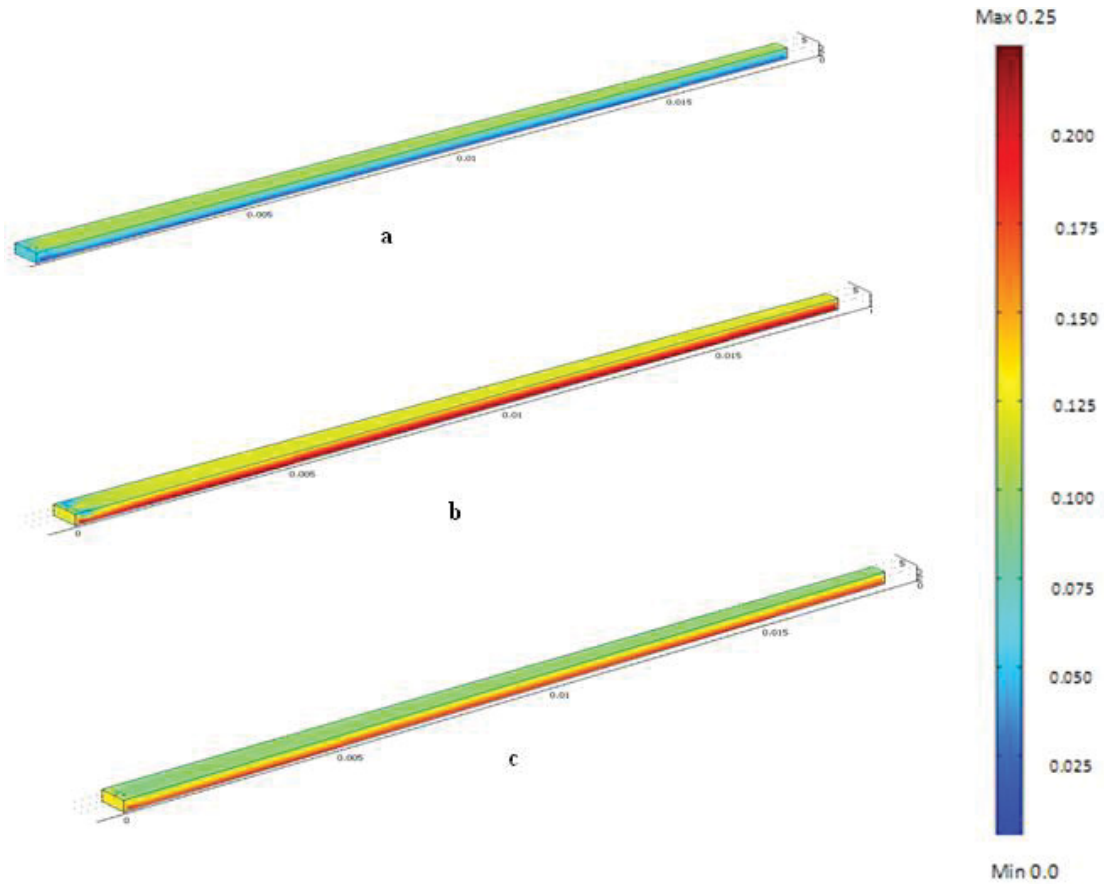
**Figure 4.11.** Concentration Distributions of Ionic Species (a) K+, (b) Fe(CN)$_6^{3-}$ (c) Fe(CN)$_6^{4-}$ in a Converging Microchannel. The concentration of the RedOx species (K$_4$[Fe(CN)$_6$]) /K$_3$[Fe(CN)$_6$]) C$_0$=0.25 M when the magnetic flux density, B =0.44 T and the dimensions of the conduit are L=18 mm, W=330 μm and H=335 μm.

### 4.2.3  Comparative Study of Velocity Profiles

A comparative study of fluid velocity vectors within each channel reveal a variation of velocity magnitude over the channel length. Due to the MHD effects, ionic fluid is pushed forward from the inlet to the outlet developing the velocity profiles over the length of the channel. As the aspect ratio (H/W) does not remain the same in case of converging and diverging channels, the development of velocity profiles is different than the straight channel in which the aspect ratio remains the same throughout the entire channel length. It should be noted that the height to the width (H/W) ratio of the straight,

63

diverging and converging channels from the inlet reservoir to the outlet reservoir are, respectively, 1 to 1, 1 to 2, and 1 to 1/2 . Two different approaches are considered to determine the effectiveness of the MHD effects in straight, diverging and converging microchannels and the models are shown in the following Figure 4.12.
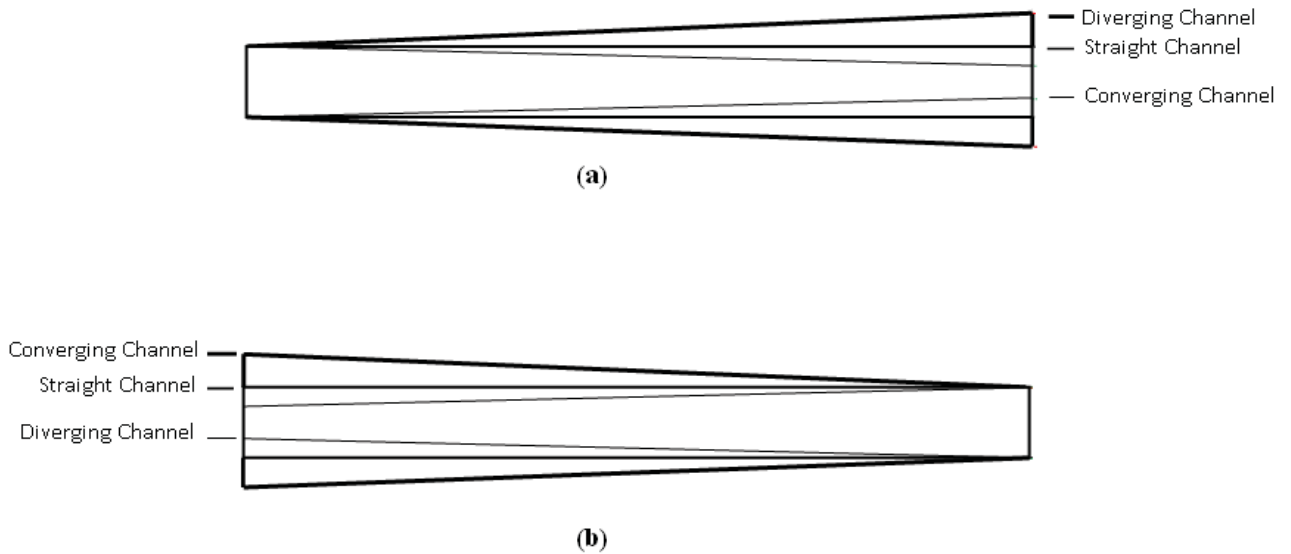


**Figure 4.12.** Three microchannel models keeping the (a) inlet cross sectional area same in all models (b) outlet cross sectional area same in all models.

One, inlet cross sectional areas are maintained the same in all the microchannel models to do a comparative study of their outlet velocities. Two, outlet cross sectional areas are maintained the same in all the microchannel models to do a comparative study of their inlet velocities. This would deliver a clear understanding of how the velocity profiles, average velocity and the maximum axial velocity change with respect to the channel height for each of the three microchannels from their inlet to mid- and to the outlet.
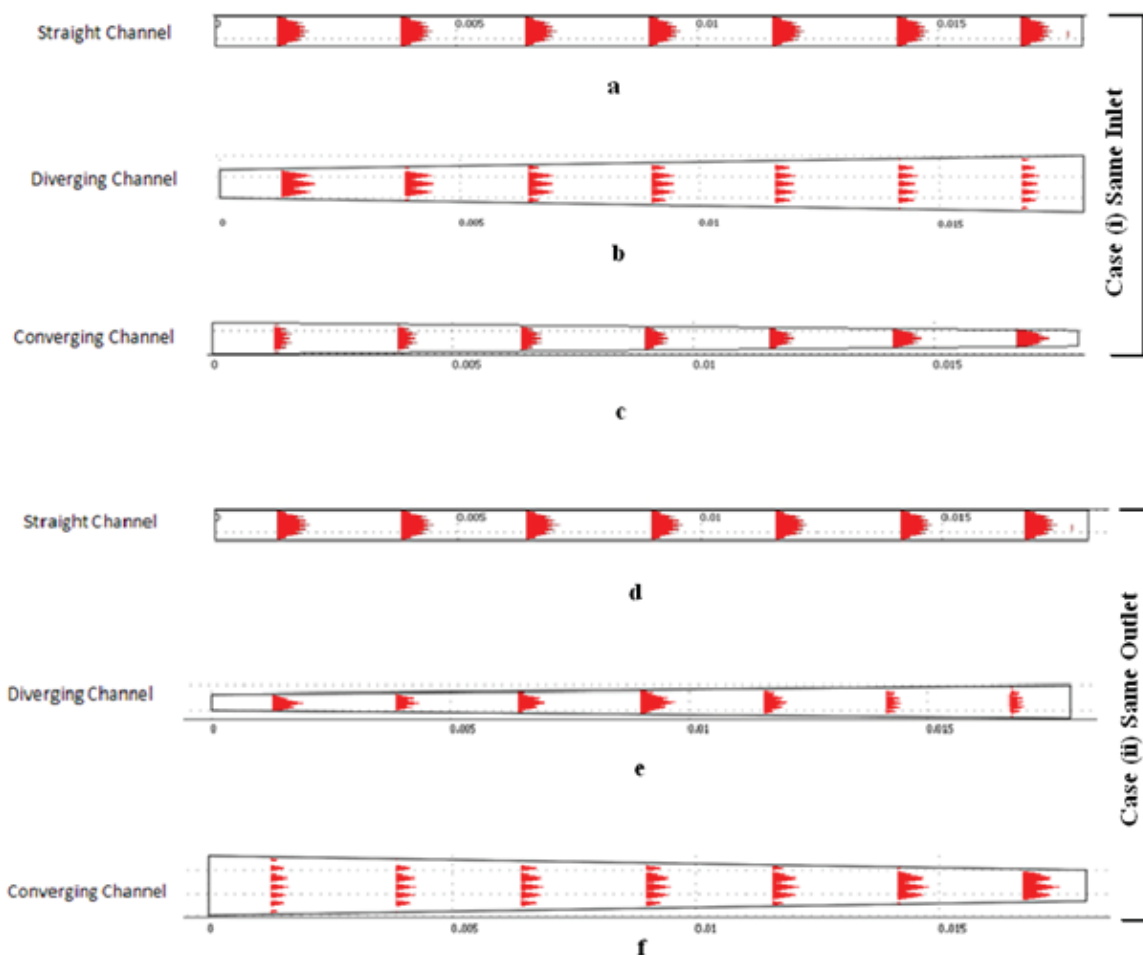
**Figure 4.13.** Velocity profiles of microchannels for case (i) same inlet assuming the cross sectional area of the inlet of the control model for all the microchannels: (a) straight (b) diverging, (c) converging microchannels and for case (ii) same outlet assuming the cross sectional area of the outlet of the control model for all the microchannels: (a) straight (b) diverging, (c) converging microchannels. The concentration of the RedOx species $(K_4[Fe(CN)_6])$ /$K_3[Fe(CN)_6])$ $C_0$=0.25 M when the magnetic flux density, B =0.44 T and the dimensions of the conduit are L=18 mm, W=330 μm and H=670 μm, 1340 μm and 335 μm for straight, diverging and converging microchannels respectively.

As shown below in Figure 4.13, in the beginning of the fluid flow, the velocity profile does not seem to be fully developed and has not reached its full velocity profile. This is due to the fact that the interaction between magnetic flux and resulting current just started from the inlet where the area of the electrode surface is minimal, so the ionic flux density is minimal and thus the fluid flow is not fully developed. This will eventually

65

create the electric double layer (EDL or Debye layer) nearby the electrodes on both walls. The velocity profiles at the inlet in all the models are shown this characteristics with more in converging, then in straight and in diverging microchannels. This is due to the reason that the outlet cross sectional area of the diverging channel is the highest among the other two models and the outlet cross sectional area of converging is the lowest.

In Figure 4.13, the arrows show the vectors of the fluid velocity in each channel and the length of the arrows presents the magnitudes of the corresponding velocity. Straight and converging channels have equal inlet height but different outlet height. In a straight channel, equal and similar trends of velocity profiles are seen as the fluid is pumping from inlet to outlet. This is due to the fact that the cross section area remains the same in inlet and outlet with a constant channel width.

In contrast, velocity magnitudes are seen increasing in the converging microchannel. This is due to the fact that the fluid is flowing from inlet to outlet, and the ratio of channel height at outlet to the height at inlet is half in order to make a converging channel. This will increase the velocity magnitude at the outlet compared to a straight channel. Similarly, velocity magnitudes are seen decreasing in the diverging microchannel which is due to the ratio of channel height at outlet to the height at inlet is twice for the diverging channel. This will decrease the velocity magnitude at the outlet.
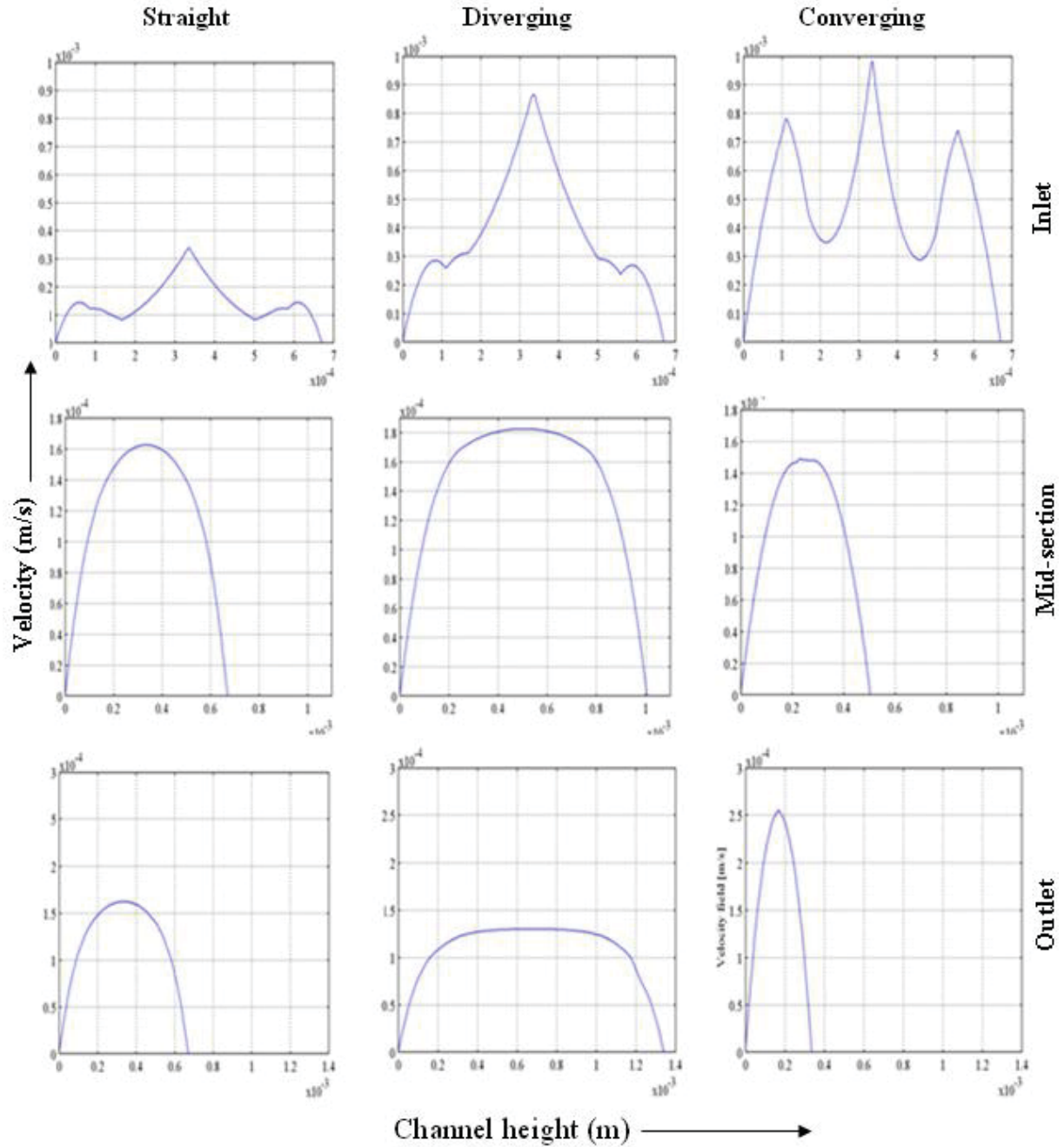
**Figure 4.14.** Velocity profiles of (i) straight, (ii) diverging, and (iii) converging microchannels assuming same inlet cross section at their (a) inlet, (b) mid-section and (c) outlet. The concentration of the RedOx species ($K_4[Fe(CN)_6]$) /$K_3[Fe(CN)_6]$) $C_0$=0.25 M when the magnetic flux density, B =0.44 T and the dimensions of the conduit are L=18 mm, W=330 μm and H=670 μm, 1340 μm and 335 μm for straight, diverging and converging microchannels respectively (Details of these figures are in the appendix).

Similar to Figure 4.13, in the beginning of the fluid flow, the velocity profile does not seem to be fully developed and has not reached its full velocity profile in Figure 4.14. This is due to the fact that the interaction between magnetic flux and resulting current just started from the inlet where the area of the electrode surface is minimal, so the ionic flux density is minimal and thus the fluid flow is not fully developed. This will eventually create the electric double layer (EDL or Debye layer) nearby the electrodes on both walls. The velocity profiles at the inlet in all the models are shown this characteristics with more in converging, then in straight and in diverging microchannels. This is due to the reason that the inlet cross sectional area of the converging channel is the highest among the other two models and the inlet cross sectional area of diverging is the lowest.

In Figure 4.14, the arrows show the vectors of the fluid velocity in each channel and the length of the arrows presents the magnitudes of the corresponding velocity. Straight and converging channels have equal outlet height but different inlet height. In a straight channel, equal and similar trends of velocity profiles are seen as the fluid is pumping from inlet to outlet. This is due to the fact that the cross section area remains the same in inlet and outlet with a constant channel width. In contrast, velocity profiles in the diverging microchannel first seems to be increasing at the mid-section then appears to be closer with the velocity profiles of the straight microchannel. Similarly, velocity profiles in the coverging microchannel gradually increasing as the flow progresses from the inlet to the mid-section and then to the outlet. The highest flow rate was observed in the converging microchannel, then in the straight and the last in the diverging microchannel. Characteristics of MHD driven fluid flow is similar to the pressure driven fluid flow in terms of the outlet velocity obtained from these three different microchannel models.
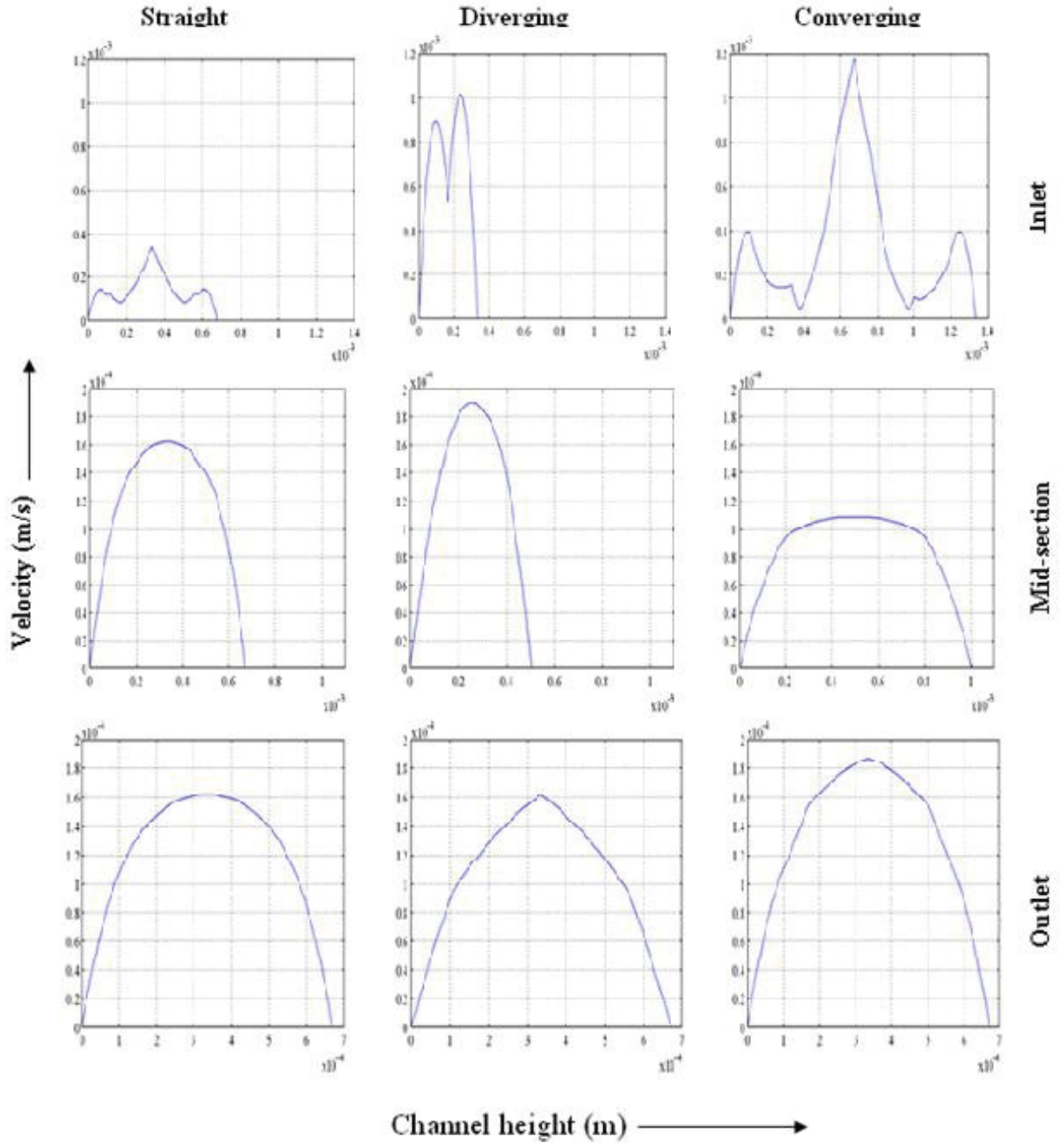
**Figure 4.15.** Velocity profiles of (i) straight, (ii) diverging, and (iii) converging microchannels assuming same outlet cross section at their (a) inlet, (b) mid-section and (c) outlet. The concentration of the RedOx species ($K_4[Fe(CN)_6]$) /$K_3[Fe(CN)_6]$) $C_0$=0.25 M when the magnetic flux density, B =0.44 T and the dimensions of the conduit are L=18 mm, W=330 μm and H=670 μm, 1340 μm and 335 μm for straight, diverging and converging microchannels respectively (Details of these figures are in the appendix).
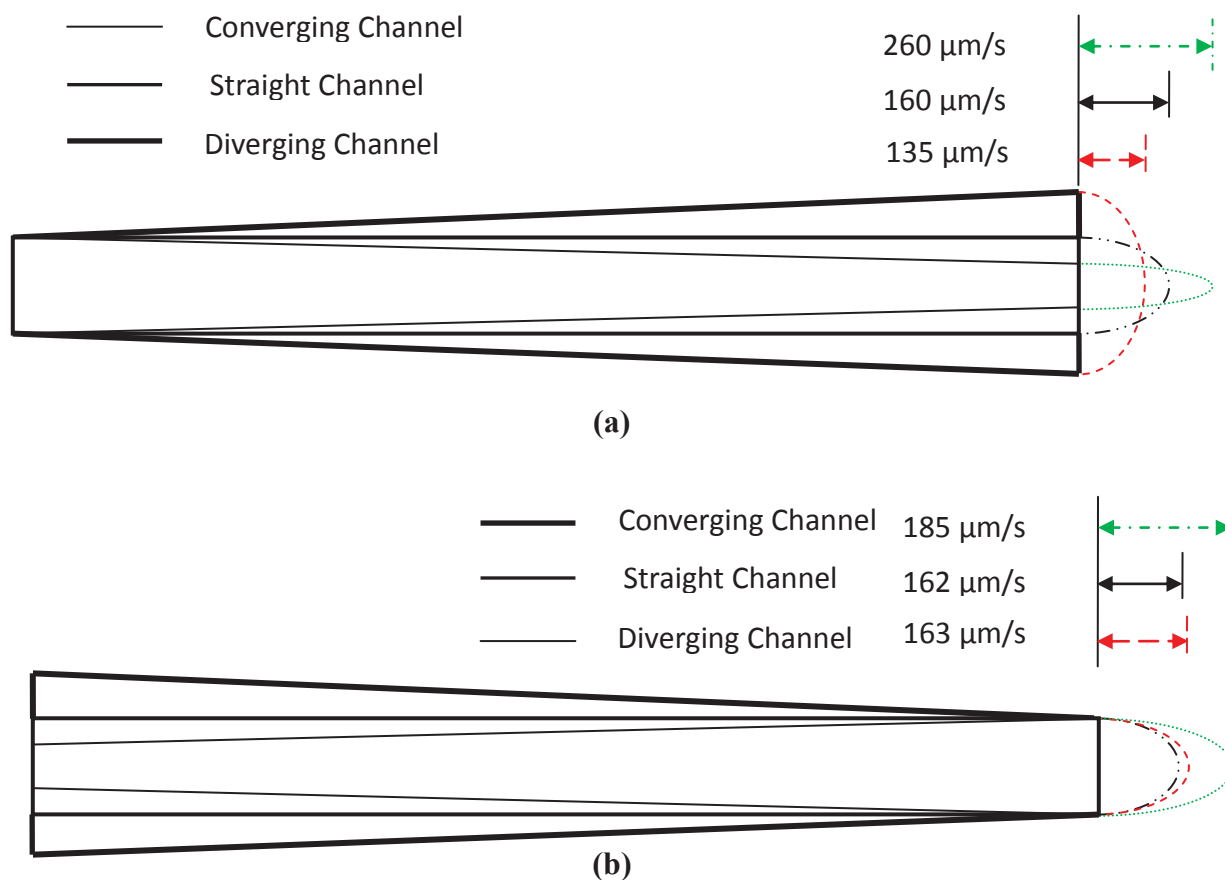
**Figure 4.16.** Outlet velocity profiles of microchannels for case (a) same inlet assuming the cross sectional area of the inlet of the control model for all the microchannels: straight diverging, converging microchannels and for case (b) same outlet assuming the cross sectional area of the outlet of the control model for all the microchannels: straight, diverging, converging microchannels. The concentration of the RedOx species $(K_4[Fe(CN)_6])$ /$K_3[Fe(CN)_6])$ $C_0$=0.25 M when the magnetic flux density, B =0.44 T and the dimensions of the conduit are L=18 mm, W=330 µm and H=670 µm, 1340 µm and 335 µm for straight, diverging and converging microchannels respectively.

As shown in the above Figure 4.15, outlet velocities from three microchannels are compared for two cases (a) same inlet cross sectional area and (b) same outlet cross sectional area. For the first case, outlet velocity of the converging microchannel is the highest and the diverging microchannel has the lowest outlet velocity. In the second scenario, both diverging and straight microchannels have almost the equal outlet

velocity.

Maximum velocity can be obtained in the converging channel, followed by straight channel, and diverging channel.

$$\bar{U} = \frac{BIH}{4\mu L\left[(n+1)\dfrac{H^2}{W^2}+(m+1)\right]}$$

(4.10)

Keeping B, I , μ, L ,W and other parameters same, varying height of the microchannel (H) affects the mean velocity $\bar{U}$ according to the above expression.

## 4.3 Conclusions

Microfluidic technology is a new and novel technique of fluid manipulation that can be used for lab-on-a -chip devices for a wide range of applications. In several micro conduits, the key problem is how to propel, manipulate, and control the fluid without using any inefficient mechanical devices. This research studied the theoretical/computational analysis of fluid manipulation by an interaction between electric and magnetic fields in various microfluidic channels. In this work, a full 3D mathematical model that consists Nernst-Planck equation (concentration of the ionic species) and Navier-Stokes equation (fluid flow performance) coupled together with various operating conditions including external magnetic field was presented. The microfluidic conduit models were based on RedOx-based MHD driven flow and the results presented here demonstrated the understanding of multiphysics flow dynamics in various microchannels with their comparative studies.

Key conclusions from this work are listed below:

1. The resulting current transmitted through the RedOx based ionic solution increases nonlinearly with the externally applied potential difference. The theoretical predictions obtained from the 3D computational simulations agree with the published experimental data.

2. The average velocity linearly increases with the increase in applied potential difference.

3. The average velocity linearly increases with the increase in the external magnetic flux densities.

4. The average velocity linearly increases with the increase of the concentrations of the RedOx ionic species.

5. The velocity is a function of physical dimensions of the micro devices.

# CHAPTER 5

# CONCLUSION AND FUTURE WORK

LOC (lab-on-a-chip) technology is the main issue for MHD (Magnetohydrodynamics) flow. This technology is widely used in many fields like mechanical, chemical, bioengineering and sensor development. And the reasons why it is important can be listed as: efficiency, low cost, convenience, difficulty of operating and reliability. However, it has some drawbacks too, and initiating and manipulating the flow is one of them. RedOx MHD can be used to solve this problem. Many works tried to study RedOx MHD mathematically, and in this paper, a 3D RedOx MHD model was created and analyzed. A full mathematical model was investigated and the inter relationship between different physical variables is studied.

## 5.1 Conclusions

In this thesis, some conclusions can be made from the results of the simulations and analysis of the mathematical model.

When the applied potential difference is low, the resulting current transmitted through the electrolyte nonlinearly increase with the potential difference. The current is a function of the magnetic flux density, concentration of RedOx species, the

dimensions of the channel, and the diffusion coefficients of the ionic species.

Similarly, the average velocity of MHD flow increases nonlinearly with the applied potential difference, but linearly increases with the current for different concentrations of the RedOx species, magnetic flux densities, and dimensions of the channel.

There is hardly an effect of the magnetic flux density on the current when the concentration of the RedOx species is low. When the concentration gets higher, the current increases with the magnetic flux density. And at the same time, the induced flow increases because of Lorentz force and the current.

## 5.2 Future Works

Despite the manipulating of the flow, there are some other drawbacks of RedOx MHD flow like bubble creation. Under high current flows, due to the electrolyte solution go through intensive electrolysis process, bubbles are generated and they will block the flow within the channel. And the other one is the corrosion of the electrodes along the channel.

So for LOC technology, these problems will be the other directions we can work on to develop this technology.

# REFERENCES

Panta Y M., Qian S., Liu J., Cheney M A., and Joo S W., *Ultrasensitive detection of mercury(II) ions using electrochemical surface plasmon with magnetohydrodynamic convection*, 2009

Panta Y M., Farmer D E., Johnson P., Cheney M A., and Qian S., *Preparation of alpha sources using magnetohydrodynamic electrodeposition for radionuclide,* 2010

Afonien Jr J.k., *Mathematical modeling of magnetohydrodynamic micropumps*, 1998.

Arumugam P., Fakunle E., Aderson E., Evans S., King K., Aguilar Z., Carter C., and Fritsch I., *Characterization and pumping RedOx magnetohydrodynamics in a microfluidic channel*, 2006.

Clark E.A., and Fritsch I., *Anodic stripping voltammetry enhancement by RedOx magnetohydrodynamics*, 2004.

COMSOL Lab., *COMSOL Multiphysics User's Guide*, 2007.

Davidson P.A., *An introduction to magnetohydrodynamics,* 2001.

Erickson D., Li D., and Park C.B., *Numerical simulations of capillary driven flows in non-uniform cross sectional capillaries*, 2002.

Erickson D., and Li D.Q., *Influence of surface heterogeneity on electrokinetically driven microfluidic mixing*, 2002.

Ho J., *Study the performance of MHD(magnetohydrodynamic) pump with the dimension of duct channel*, 2007

Jang J., and Lee S.S., *Theoretical and experimental study of MHD (magnetohydrodynamic) micropump*, 2000

Johnson R.D., Badr I.H.A., Barrett G., Lai S.Y., Lu Y.M., Madou M.J. and Bachas L.G., *Development of a fully integrated analysis system for ions based on ion-selective optodes and centrifugal microfluidics*, 2001.

Kabbani H., *Magnetohydrodynamics in microchannels and adhesion properties of nanoporous alumina films*, 2005

Leventis N., and Gao X.R., *Steady-state voltammetry with stationary fisk millielectrodes in magnetic field: Nonlinear dependence of the mass-transfer limited current on the electron balance of the Faradaic process,* 1999.

Qian S., and Bau H.H., *Magnet-hydrodynamics based microfluidics*, Volume 36, Issue 1, 2009.

Qian S., and Bau H.H., *Magneto-hydrodynamic flow of RedOx electrolyte*, 2005.

Qian S., Zhu J., Xiang Y., and Bau H.H., *A Magneto-hydrodynamic micro fluidic network*, 2002.

West J., Karamata B., Lillis B., Gleeson J.P., Alderman J., Collins J.K., Lane W., and Mathewson A., *Application of magnetohydrodynamic actuation to continuous flow chemistry*, 2002

Wheeler A.R., Throndset W.R., Whelan R.J., Leach A.M., Zare R.N., Liao Y.H., Farrell K., Manger I.D., and Daridon A., *Microfluidic device for single-cell analysis,* 2003

Vladimirova N., Malagoli A., and Mauri R., *Diffusionphoresis of two-dimensional liquid droplets in a phase-separating system*, 1999.

Zhong J.H., Yi M.Q., Bau H.H., *Magnetohydrodynamic(MHD) pomp fabricated with ceramic lapes*, 2002